Nonlinear Dynamics of Nanomechanical and Micromechanical Resonators

Preprint of contribution to:

Review of Nonlinear Dynamics and Complexity,
Edited by Heinz Georg Schuster (Wiley, 2008)

Ron Lifshitz and M. C. Cross

March 5, 2008

Contents

1
Nonlinear Dynamics of Nanomechanical and Micromechanical Resonators

1.1
Nonlinearities in NEMS and MEMS resonators

In the last decade we have witnessed exciting technological advances in the fabrication and control of microelectromechanical and nanoelectromechanical systems (MEMS & NEMS) [1–5]. Such systems are being developed for a host of nanotechnological applications, such as highly-sensitive mass [6–8], spin [9], and charge detectors [10,11], as well as for basic research in the mesoscopic physics of phonons [12], and the general study of the behavior of mechanical degrees of freedom at the interface between the quantum and the classical worlds [13, 14]. Surprisingly, MEMS & NEMS have also opened up a whole new experimental window into the study of the nonlinear dynamics of discrete systems in the form of nonlinear micromechanical and nanomechanical oscillators and resonators.

The purpose of this review is to provide an introduction to the nonlinear dynamics of micromechanical and nanomechanical resonators that starts from the basics, but also touches upon some of the advanced topics that are relevant for current experiments with MEMS & NEMS devices. We begin in this section with a general motivation, explaining why nonlinearities are so often observed in NEMS & MEMS devices. In § 1.2 we describe the dynamics of one of the simplest nonlinear devices—the Duffing resonator—while giving a tutorial in secular perturbation theory as we calculate its response to an external drive. We continue to use the same analytical tools in § 1.3 to discuss the dynamics of a parametrically-excited Duffing resonator, building up to the description of the dynamics of an array of coupled parametrically-excited Duffing resonators in § 1.4. We conclude in § 1.5 by giving an amplitude equation description for the array of coupled Duffing resonators, allowing us to extend our analytic capabilities in predicting and explaining the nature of its dynamics.

1.1.1
Why study nonlinear NEMS and MEMS?

Interest in the nonlinear dynamics of microelectromechanical and nanoelectromechanical systems (MEMS & NEMS) has grown rapidly over the last few years, driven by a

combination of practical needs as well as fundamental questions. Nonlinear behavior is readily observed in micro- and nano-scale mechanical devices [3, 15–32]. Consequently, there exists a practical need to understand this behavior in order to avoid it when it is unwanted, and exploit it efficiently when it is wanted. At the same time, advances in the fabrication, transduction, and detection of MEMS & NEMS resonators has opened up an exciting new experimental window into the study of fundamental questions in nonlinear dynamics. Typical nonlinear MEMS & NEMS resonators are characterized by extremely high frequencies—recently going beyond 1 GHz [33–35]—and relatively weak dissipation, with quality factors in the range of $10^2 - 10^4$. For such devices the regime of physical interest is that of steady state motion as transients tend to disappear before they are detected. This, and the fact that weak dissipation can be treated as a small perturbation, provide a great advantage for quantitative theoretical study. Moreover, the ability to fabricate arrays of tens to hundreds of coupled resonators opens new possibilities in the study of nonlinear dynamics of intermediate numbers of degrees of freedom—much larger than one can study in macroscopic or table-top experiments, yet much smaller than one studies when considering nonlinear aspects of phonon dynamics in a crystal. The collective response of coupled arrays might be useful for signal enhancement and noise reduction [36], as well as for sophisticated mechanical signal processing applications. Such arrays have already exhibited interesting nonlinear dynamics ranging from the formation of extended patterns [37]—as one commonly observes in analogous continuous systems such as Faraday waves—to that of intrinsically localized modes [38–40]. Thus, nanomechanical resonator arrays are perfect for testing dynamical theories of discrete nonlinear systems with many degrees of freedom. At the same time, the theoretical understanding of such systems may prove useful for future nanotechnological applications.

1.1.2
Origin of nonlinearity in NEMS and MEMS resonators

We are used to thinking about mechanical resonators as being simple harmonic oscillators, acted upon by linear elastic forces that obey Hooke's law. This is usually a very good approximation as most materials can sustain relatively large deformations before their intrinsic stress-strain relation breaks away from a simple linear description. Nevertheless, one commonly encounters nonlinear dynamics in micromechanical and nanomechanical resonators long before the intrinsic nonlinear regime is reached. Most evident are nonlinear effects that enter the equation of motion in the form of a force that is proportional to the cube of the displacement αx^3. These turn a simple harmonic resonator with a linear restoring force into a so-called Duffing resonator. The two main origins of the observed nonlinear effects are illustrated below with the help of two typical examples. These are due to the effect of external potentials that are often nonlinear, and geometric effects that introduce nonlinearities even though the individual forces that are involved are all linear. The Duffing nonlinearity αx^3 can be positive, assisting
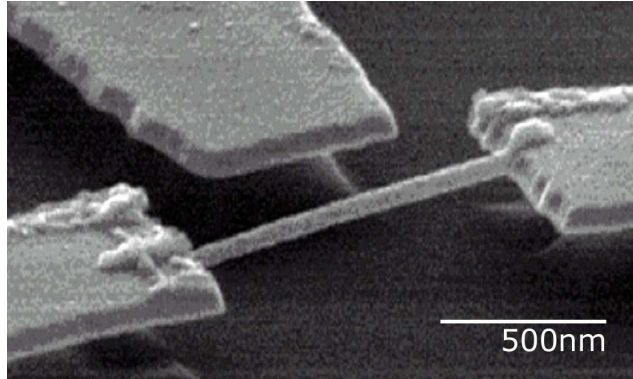
Fig. 1.1 A 43 nanometer thick doubly-clamped platinum nanowire with an external electrode that can be used to tune its natural frequency as well as its nonlinear properties. Adapted with permission from Refs. [30].

the linear restoring force, making the resonator stiffer, and increasing its resonance frequency. It can also be negative, working against the linear restoring force, making the resonator softer, and decreasing its resonance frequency. The two examples we give below illustrate how both of these situations can arise in realistic MEMS & NEMS devices.

Additional sources of nonlinearity may be found in experimental realizations of MEMS and NEMS resonators due to practical reasons. These may include nonlinearities in the actuation and in the detection mechanisms that are used for interacting with the resonators. There could also be nonlinearities that result from the manner in which the resonator is clamped by its boundaries to the surrounding material. These all introduce external factors that may contribute to the overall nonlinear behavior of the resonator.

Finally, nonlinearities often appear in the damping mechanisms that accompany every physical resonator. We shall avoid going into the detailed description of the variety of physical processes that govern the damping of a resonator. Suffice it to say that whenever it is reasonable to expand the forces acting on a resonator up to the cube of the displacement x^3, it should correspondingly be reasonable to add to the linear damping which is proportional to the velocity of the resonator $\dot{x}$, a nonlinear damping term of the form $x^2\dot{x}$, which increases with the amplitude of motion. Such nonlinear damping will be considered in our analysis below.

1.1.3
Nonlinearities arising from external potentials

As an example of the effect of an external potential, let us consider a typical situation, discussed for example by Cleland and Roukes [10, 11], and depicted in Fig. 1.1, in

which a harmonic oscillator is acted upon by an external electrostatic force. This could be implemented by placing a rigid electrically-charged base electrode near an oppositely-charged NEMS or MEMS resonator. If the equilibrium separation between the resonator and the base electrode in the absence of electric charge is d, the deviation away from this equilibrium position is denoted by X, the effective elastic spring constant of the resonator is K, and the charge q on the resonator is assumed to be constant, then the potential energy of the resonator is given by

$$V(X) = \frac{1}{2}KX^2 - \frac{C}{d+X} . \tag{1.1}$$

In SI units $C = Aq^2/4\pi\epsilon_0$, where A is a numerical factor of order unity that takes into account the finite dimensions of the charged resonator and base electrode. The new equilibrium position X_0 in the presence of charge can be determined by solving the cubic equation

$$\frac{dV}{dX} = KX + \frac{C}{(d+X)^2} = 0. \tag{1.2}$$

If we now expand the potential acting on the resonator in a power series in the deviation $x = X - X_0$ from this new equilibrium we obtain

$$\begin{aligned} V(x) &\simeq V(X_0) + \frac{1}{2}\left(K - \frac{2C}{(d+X_0)^3}\right)x^2 + \frac{C}{(d+X_0)^4}x^3 - \frac{C}{(d+X_0)^5}x^4 \\ &= V(X_0) + \frac{1}{2}kx^2 + \frac{1}{3}\beta x^3 + \frac{1}{4}\alpha x^4. \end{aligned} \tag{1.3}$$

This gives rise, without any additional driving or damping, to an equation of motion of the form

$$m\ddot{x} + kx + \beta x^2 + \alpha x^3 = 0, \qquad \text{with} \quad \beta > 0, \, \alpha < 0, \tag{1.4}$$

where m is the effective mass of the resonator; k is its new effective spring constant, which is softened by the electrostatic attraction to the base electrode, but note that if $2C/(d+X_0)^3 > K$, the electrostatic force exceeds the elastic restoring force and the resonator is pulled onto the base electrode; β is a positive symmetry-breaking quadratic elastic constant that pulls the resonator towards the base electrode regardless of the sign of x; and α is the cubic, or Duffing, elastic constant that owing to its negative sign softens the effect of the linear restoring force. It should be sufficient to stop the expansion here, unless the amplitude of the motion is much larger than the size of the resonator, or if by some coincidence the effects of the quadratic and cubic nonlinearities happen to cancel each other out—a situation that will become clearer after reading § 1.2.3.

1.1.4
Nonlinearities due to geometry

As an illustration of how nonlinearities can emerge from linear forces due to geometric effects, consider a doubly-clamped thin elastic beam, which is one of the most commonly encountered NEMS resonators. Because of the clamps at both ends, as the beam deflects in its transverse motion it necessarily stretches. As long as the amplitude of the transverse motion is much smaller than the width of the beam this effect can be neglected. But with NEMS beams it is often the case that they are extremely thin, and are driven quite strongly, making it common for the amplitude of vibration to exceed the width. Let us consider this effect in some detail by starting with the Euler-Bernoulli equation, which is the commonly used approximate equation of motion for a thin beam [41]. For a transverse displacement $X(z,t)$ from equilibrium, which is much smaller than the length L of the beam, the equation is

$$\rho S \frac{\partial^2 X}{\partial t^2} = -EI \frac{\partial^4 X}{\partial z^4} + T \frac{\partial^2 X}{\partial z^2}, \tag{1.5}$$

where z is the coordinate along the length of the beam; ρ the mass density; S the area of the cross section of the beam; E the Young modulus; I the moment of inertia; and T the tension in the beam, which is composed of its inherent tension T_0 and the additional tension ΔT due to its bending that induces an extension ΔL in the length of the beam. Inherent tension results from the fact that in equilibrium in the doubly-clamped configuration, the actual length of the beam may differ form its rest length being either extended (positive T_0) or compressed (negative T_0). The additional tension ΔT is given by the strain, or relative extension of the beam $\Delta L / L$ multiplied by Young's modulus E and the area of the beam's cross section S. For small displacements the total length of the beam can be expanded as

$$L + \Delta L = \int_0^L dz \sqrt{1 + \left(\frac{\partial X}{\partial z}\right)^2} \simeq L + \frac{1}{2} \int_0^L dz \left(\frac{\partial X}{\partial z}\right)^2. \tag{1.6}$$

The equation of motion (1.5) then clearly becomes nonlinear

$$\rho S \frac{\partial^2 X}{\partial t^2} = -EI \frac{\partial^4 X}{\partial z^4} + \left[T_0 + \frac{ES}{2L} \int_0^L dz \left(\frac{\partial X}{\partial z}\right)^2\right] \frac{\partial^2 X}{\partial z^2}. \tag{1.7}$$

We can treat this equation perturbatively [42, 43]. We consider first the linear part of the equation, which has the form of Eq. (1.5) with T_0 in place of T, separate the variables,

$$X_n(z,t) = x_n(t)\phi_n(z), \tag{1.8}$$

and find its spatial eigenmodes $\phi_n(z)$, where we use the convention that the local maximum of the eigenmode $\phi_n(z)$ that is nearest to the center of the beam is scaled

to 1. Thus $x_n(t)$ measures the actual deflection at the point nearest to its center that extends the furthest. Next, we assume that the beam is vibrating predominantly in one of these eigenmodes and use this assumption to evaluate the effective Duffing parameter α_n, multiplying the x_n^3 term in the equation of motion for this mode. Corrections to this approximation will appear only at higher orders of x_n. We multiply Eq. (1.7) by the chosen eigenmode $\phi_n(z)$, and integrate over z to get, after some integration by parts, a Duffing equation of motion for the amplitude of the nth mode $x_n(t)$,

$$\ddot{x}_n + \left[\frac{EI}{\rho S} \frac{\int \phi_n''^2 dz}{\int \phi_n^2 dz} + \frac{T_0}{\rho S} \frac{\int \phi_n'^2 dz}{\int \phi_n^2 dz} \right] x_n + \left[\frac{E}{2\rho L} \frac{\left(\int \phi_n'^2 dz \right)^2}{\int \phi_n^2 dz} \right] x_n^3 = 0, \tag{1.9}$$

where primes denote derivatives with respect to z, and all the integrals are from 0 to L. Note that we have obtained a positive Duffing term, indicating a stiffening non-linearity, as opposed to the softening nonlinearity that we saw in the previous section. Also note that the effective spring constant can be made negative by compressing the equilibrium beam, thus making T_0 large and negative. This may lead to the so-called Euler instability, which is a buckling instability of the beam.

To evaluate the effective Duffing nonlinearity α_n for the nth mode, we introduce a dimensionless parameter $\hat{\alpha}_n$ by rearranging the equation of motion (1.9), to have the form

$$\ddot{x}_n + \omega_n^2 x_n \left[1 + \hat{\alpha}_n \frac{x_n^2}{d^2} \right] = 0, \tag{1.10}$$

where ω_n is the normal frequency of the nth mode, d is the width, or diameter, of the beam in the direction of the vibration, and x_n is the maximum displacement of the beam near its center. This parameter can then be evaluated regardless of the actual dimension of the beam.

In the limit of small residual tension T_0 the eigenmodes are those dominated by bending given by [41]

$$\begin{aligned} \phi_n(z) = \quad & \frac{1}{a_n} \left[(\sin k_n L - \sinh k_n L)(\cos k_n z - \cosh k_n z) \right. \\ & \left. - (\cos k_n L - \cosh k_n L)(\sin k_n z - \sinh k_n z) \right], \end{aligned} \tag{1.11}$$

where a_n is the value of the function in the square brackets at its local maximum that is closest to $z = 0.5$, and the wave vectors k_n are solutions of the transcendental equation $\cos k_n L \cosh k_n L = 1$. The first few values are

$$\{k_n L\} \simeq \{4.7300, 7.8532, 10.9956, 14.1372, 17.2788, 20.4204 \ldots\}, \tag{1.12}$$

and the remaining ones tend towards odd-integer multiples of $\pi/2$, as n increases. Using these eigenfucntion we can obtain explicit values for the dimensionless Duffing parameters for the different modes, by calculating

$$\hat{\alpha}_n = \frac{Sd^2}{2I} \frac{\left(\frac{1}{L} \int \phi_n'^2 dz \right)^2}{\frac{1}{L} \int \phi_n''^2 dz} \equiv \frac{Sd^2}{2I} \hat{\beta}_n. \tag{1.13}$$

The first few values are

$$\left\{\hat{\beta}_n\right\} \simeq \{0.1199, 0.2448, 0.3385, 0.3706, 0.3908, 0.4068, 0.4187, \ldots\}, \qquad (1.14)$$

tending to an asymptotic value of $1/2$ as $n \to \infty$. For beams with rectangular or circular cross sections, the geometric prefactor evaluates to

$$\frac{Sd^2}{2I} = \begin{cases} 16 & \text{Circular cross section}, \\ 6 & \text{Rectangular cross section}. \end{cases} \qquad (1.15)$$

Thus the dimensionless Duffing parameters are of order 1, and therefore the significance of the nonlinear behavior is solely determined by the ratio of the deflection to the width of the beam.

In the limit of large equilibrium tension, the beam essentially behaves as a string with relatively negligible resistance to bending. The eigenmodes are those of a string,

$$\phi_n(z) = \sin\left(\frac{n\pi}{L}z\right), \quad n = 1, 2, 3\ldots, \qquad (1.16)$$

and, if we denote the equilibrium extension of the beam as $\Delta L_0 = LT_0/ES$, the dimensionless Duffing parameters are exactly given by

$$\hat{\alpha}_n = \frac{d^2}{2\Delta L_0} \int \phi_n'^2 dz = \frac{(n\pi d)^2}{4L\Delta L_0}. \qquad (1.17)$$

In the large tension limit, as in the case of a string, the dimensionless Duffing parameters are proportional to the inverse aspect ratio of the beam d/L times the ratio between its width and the extension from its rest length $d/\Delta L_0$, at least one of which can be a very small parameter. For this reason nonlinear effects are relatively negligible in these systems.

1.2
The directly-driven damped Duffing resonator

1.2.1
The scaled Duffing equation of motion

Let us begin by considering a single nanomechanical Duffing resonator with linear and nonlinear damping that is driven by an external sinusoidal force. We shall start with the common situation where there is symmetry between x and $-x$, and consider later the changes that are introduced by adding symmetry-breaking terms. Such a resonator is described by the equation of motion

$$m\frac{d^2\tilde{x}}{d\tilde{t}^2} + \Gamma\frac{d\tilde{x}}{d\tilde{t}} + m\omega_0^2\tilde{x} + \tilde{\alpha}\tilde{x}^3 + \tilde{\eta}\tilde{x}^2\frac{d\tilde{x}}{d\tilde{t}} = \tilde{G}\cos\tilde{\omega}\tilde{t}, \qquad (1.18)$$

where m is its effective mass, $k = m\omega_0^2$ is its effective spring constant, $\tilde{\alpha}$ is the cubic spring constant, or Duffing parameter, Γ is the linear damping rate, and $\tilde{\eta}$ is the coefficient of nonlinear damping—damping that increases with the amplitude of oscillation. We follow the convention that physical parameters that are immediately rescaled appear with twiddles, as the first step in dealing with such an equation is to scale away as many unnecessary parameters as possible, leaving only those that are physically-significant, thus removing all of the twiddles. We do so by: (1) Measuring time in units of ω_0^{-1} so that the dimensionless time variable is $t = \omega_0 \tilde{t}$. (2) Measuring amplitudes of motion in units of length for which a unit-amplitude oscillation doubles the frequency of the resonator. This is achieved by taking the dimensionless length variable to be $x = \tilde{x}\sqrt{\tilde{\alpha}/m\omega_0^2}$. For the doubly-clamped beam of width or diameter d, discussed in § 1.1.4, this length is $x = \tilde{x}\sqrt{\hat{\alpha}_n}/d$. (3) Dividing the equation by an overall factor of $\omega_0^3\sqrt{m^3/\tilde{\alpha}}$. This yields a scaled Duffing equation of the form

$$\ddot{x} + Q^{-1}\dot{x} + x + x^3 + \eta x^2 \dot{x} = G\cos\omega t, \tag{1.19}$$

where dots denote derivatives with respect to the dimensionless time t, all the dimensionless parameters are related to the physical ones by

$$Q^{-1} = \frac{\Gamma}{m\omega_0}; \quad \eta = \frac{\tilde{\eta}\omega_0}{\tilde{\alpha}}; \quad G = \frac{\tilde{G}}{\omega_0^3}\sqrt{\frac{\tilde{\alpha}}{m^3}}; \quad \text{and} \quad \omega = \frac{\tilde{\omega}}{\omega_0}; \tag{1.20}$$

and Q is the quality factor of the resonator.

1.2.2
A solution using secular perturbation theory

We proceed to calculate the response of the damped Duffing resonator to an external sinusoidal drive, as given by Eq. (1.19), by making use of secular perturbation theory [44, 45]. We do so in the limit of a weak linear damping rate Q^{-1}, which we use to define a small expansion parameter, $Q^{-1} \equiv \epsilon \ll 1$. In most actual applications Q is at least on the order of 100, thus taking this limit is well-justified. We also consider the limit of weak oscillations where it is justified to truncate the expansion of the force acting on the resonator at the third power of x. We do so by requiring that the cubic force x^3 be a factor of ϵ smaller than the linear force, or equivalently, by requiring the deviation from equilibrium x to be on the order of $\sqrt{\epsilon}$. We ensure that the external driving force has the right strength to induce such weak oscillations by having it enter the equation at the same order as all the other physical effects. This turns out to require the amplitude of the drive to be $G = \epsilon^{3/2}g$. To see why, recall that for a regular linear resonance x is proportional to GQ. Here we want x to be of order $\sqrt{\epsilon}$, and Q is of order ϵ^{-1}, thus G has to be of order $\epsilon^{3/2}$. Finally, since damping is weak we expect to see response only close to the resonance frequency. We therefore take the driving frequency to be of the form $\omega = 1 + \epsilon\Omega$. The equation of motion (1.19) therefore

becomes

$$\ddot{x} + \epsilon \dot{x} + x + x^3 + \eta x^2 \dot{x} = \epsilon^{3/2} g \cos(1 + \epsilon \Omega) t. \tag{1.21}$$

This is the equation we shall study using secular perturbation theory, while comparing from time to time back to the original physical equation (1.18).

Expecting the motion of the resonator away from equilibrium to be on the order of $\epsilon^{1/2}$, we try a solution of the form

$$x(t) = \frac{\sqrt{\epsilon}}{2} \left(A(T) e^{it} + c.c. \right) + \epsilon^{3/2} x_1(t) + \ldots, \tag{1.22}$$

where $c.c.$ denotes complex conjugation. The lowest order contribution to this solution is based on the solution to the linear equation of motion of a simple harmonic oscillator (SHO) $\ddot{x} + x = 0$, where $T = \epsilon t$ is a slow time variable, allowing the complex amplitude $A(T)$ to vary slowly in time, due to the effect of all the other terms in the equation. As we shall immediately see, the slow temporal variation of $A(T)$ also allows us to ensure that the perturbative correction $x_1(t)$, as well as all higher-order corrections to the linear equation, do not diverge (as they do if one uses naive perturbation theory). Using the relation

$$\dot{A} = \frac{dA}{dt} = \epsilon \frac{dA}{dT} \equiv \epsilon A', \tag{1.23}$$

we calculate the time derivatives of the trial solution (1.22)

$$\dot{x} = \frac{\sqrt{\epsilon}}{2} \left([iA + \epsilon A'] e^{it} + c.c. \right) + \epsilon^{3/2} \dot{x}_1(t) + \ldots \tag{1.24a}$$

$$\ddot{x} = \frac{\sqrt{\epsilon}}{2} \left([-A + 2i\epsilon A' + \epsilon^2 A''] e^{it} + c.c. \right) + \epsilon^{3/2} \ddot{x}_1(t) + \ldots \tag{1.24b}$$

By substituting these expressions back into the equation of motion (1.21), and picking out all terms of order $\epsilon^{3/2}$, we get the following equation for the first perturbative correction

$$\ddot{x}_1 + x_1 = \left(-iA' - i\frac{1}{2}A - \frac{3 + i\eta}{8} |A|^2 A + \frac{g}{2} e^{i\Omega T} \right) e^{it} - \frac{1 + i\eta}{8} A^3 e^{3it} + c.c. \tag{1.25}$$

The collection of terms proportional to e^{it} on the right-hand side of Eq. (1.25), called the secular terms, act like a force, driving the SHO on the left-hand side exactly at its resonance frequency. The sum of all these terms must therefore vanish so that the perturbative correction $x_1(t)$ will not diverge. This requirement is the so-called "solvability condition", giving us an equation for determining the slowly varying amplitude $A(T)$,

$$\frac{dA}{dT} = -\frac{1}{2}A + i\frac{3}{8}|A|^2 A - \frac{\eta}{8}|A|^2 A - i\frac{g}{2} e^{i\Omega T}. \tag{1.26}$$

This general equation could be used to study many different effects [46]. Here we use it to study the steady-state dynamics of the driven Duffing resonator.

We ignore initial transients, and assume that a steady-state solution of the form

$$A(T) = ae^{i\Omega T} \equiv |a|e^{i\phi}e^{i\Omega T} \tag{1.27}$$

exists. With this expression for the slowly varying amplitude $A(T)$ the solution to the original equation of motion (1.21) becomes an oscillation at the drive frequency $\omega = 1 + \epsilon\Omega$,

$$x(t) = \epsilon^{1/2}|a|\cos(\omega t + \phi) + O(\epsilon^{3/2}), \tag{1.28}$$

where we are not interested in the actual correction $x_1(t)$ of order $\epsilon^{3/2}$, but rather in finding the fixed complex amplitude a of the lowest order term. This amplitude a can be any solution of the equation

$$\left[\left(\frac{3}{4}|a|^2 - 2\Omega\right) + i\left(1 + \frac{\eta}{4}|a|^2\right)\right]a = g, \tag{1.29}$$

obtained by substituting the steady-state solution (1.27) into Eq. (1.26) of the secular terms.

The magnitude and phase of the response are then given explicitly by

$$|a|^2 = \frac{g^2}{\left(2\Omega - \frac{3}{4}|a|^2\right)^2 + \left(1 + \frac{1}{4}\eta|a|^2\right)^2}, \tag{1.30a}$$

and

$$\tan\phi = \frac{1 + \frac{1}{4}\eta|a|^2}{2\Omega - \frac{3}{4}|a|^2}. \tag{1.30b}$$

By reintroducing the original physical scales we can obtain the physical solution to the original equations of motion, $\tilde{x}(\tilde{t}) \simeq \tilde{x}_0 \cos(\tilde{\omega}\tilde{t} + \phi)$, where $\tilde{x}_0 = |a|\sqrt{\Gamma\omega_0/\tilde{\alpha}}$, and therefore

$$\tilde{x}_0^2 = \frac{\left(\frac{\tilde{G}}{2m\omega_o^2}\right)^2}{\left(\frac{\tilde{\omega}-\omega_0}{\omega_0} - \frac{3}{8}\frac{\tilde{\alpha}}{m\omega_0^2}\tilde{x}_0^2\right)^2 + (\frac{1}{2}Q^{-1} + \frac{1}{8}\frac{\tilde{\eta}}{m\omega_0}\tilde{x}_0^2)^2} \tag{1.31a}$$

and

$$\tan\phi = \frac{\frac{\Gamma}{2} + \frac{\tilde{\eta}}{8}\tilde{x}_0^2}{m\tilde{\omega} - m\omega_0 - \frac{3\tilde{\alpha}}{8\omega_0}\tilde{x}_0^2}. \tag{1.31b}$$

The scaled response functions (1.30) are plotted in Fig. 1.2 for a drive with a scaled amplitude of $g = 3$ with and without nonlinear damping. The response without nonlinear damping is shown also in Fig. 1.3 for a sequence of increasing drive amplitudes
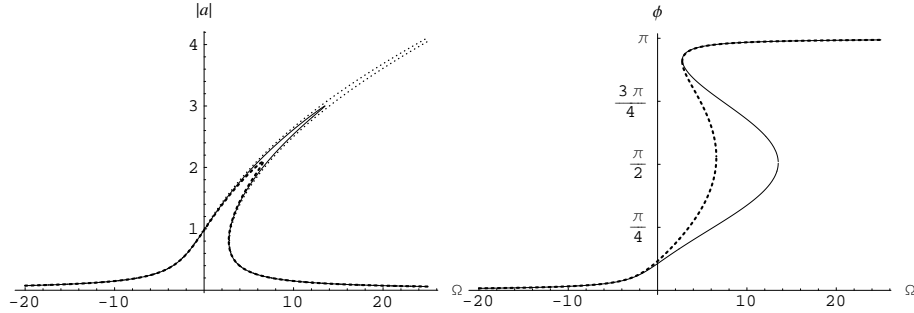
Fig. 1.2 Magnitude $|a|$ (left) and phase ϕ (right) of the response of a Duffing resonator as a function of the frequency Ω, for a fixed driving amplitude $g = 3$. The thin solid curves show the response without any nonlinear damping ($\eta = 0$). The thick dotted curves show the response with nonlinear damping ($\eta = 0.1$). The thin dotted curve on the left shows the response without any kind of damping [$Q^{-1} = 0$ and $\eta = 0$ in the original equation (1.19)]. The phase in this case is 0 along the whole upper-left branch and π along the whole lower-right branch, and so is not plotted on the right.

ranging from $g = 0.1$, where the response is essentially linear, to the value of $g = 4$. Note that due to our choice of a positive Duffing nonlinearity the resonator becomes stiffer and its frequency higher as the amplitude increases. The response amplitude of the driven resonator therefore increases with increasing frequency, until it reaches a saddle-node bifurcation and drops abruptly to zero. A negative Duffing parameter would produce a mirror image of this response curve.

One sees that the magnitude of the response, given by Eq. (1.30a), formally-approaches the Lorentzian response of a linear SHO if we let the nonlinear terms in the original equation of motion tend to zero. Their existence modifies the response function with the appearance of the squared magnitude $|a|^2$ in the denominator on the right-hand side of Eq. (1.30a), turning the solution into a cubic polynomial in $|a|^2$. As such there are either one or three real solutions for $|a|^2$, and therefore for $|a|$, as a function of either the drive amplitude g or the driving frequency Ω. We shall analyze the dependence of the magnitude of the response on frequency in some detail, and leave it to the reader to perform a similar analysis of the dependence on drive amplitude, which is very similar.

In order to analyze the magnitude of the response $|a|$ as a function of driving frequency Ω let us differentiate the response function (1.30a),

$$\left[\frac{3}{64}\left(9 + \eta^2\right)|a|^4 + \frac{1}{4}\left(\eta - 6\Omega\right)|a|^2 + \frac{1}{4} + \Omega^2\right]d|a|^2 = \left[\frac{3}{4}|a|^4 - 2\Omega|a|^2\right]d\Omega.$$
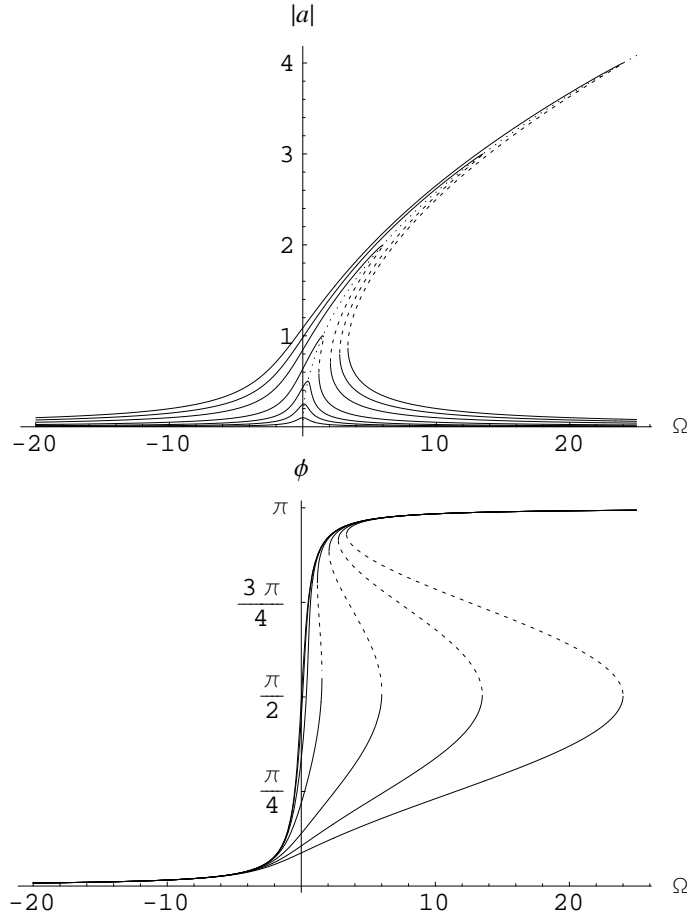
$$(1.32)$$

Fig. 1.3 Magnitudes $|a|$ (top) and phases ϕ (bottom) of the response of a Duffing resonator as a function of the frequency Ω, for a sequence of increasing values of the drive amplitude $0.1 \leq g \leq 4.0$, without nonlinear damping ($\eta = 0$). Solid curves indicate stable solutions of the response function (1.30), while dashed curves indicate unstable solutions.

This allows us immediately to find the condition for resonance, where the magnitude of the response is at its peak, by requiring that $d|a|^2/d\Omega = 0$. We find that the resonance frequency Ω_{max} depends quadratically on the peak magnitude $|a|_{max}$, according to

$$\Omega_{max} = \frac{3}{8}|a|^2_{max}, \tag{1.33a}$$

or in terms of the original variables as

$$\tilde{\omega}_{max} = \omega_0 + \frac{3}{8}\frac{\alpha}{m\omega_0}(\tilde{x}_0)^2_{max}. \tag{1.33b}$$

The curve, satisfying Eq. (1.33a), for which $|a| = \sqrt{8\Omega/3}$, is plotted in Fig. 1.3. It forms a square-root back-bone that connects all the resonance peaks for the different driving amplitudes, which is often seen in typical experiments with nanomechanical resonators. Thus the peak of the response is pulled further toward higher frequencies as the driving amplitude g is increased, as expected from a stiffening nonlinearity.

When the drive amplitude g is sufficiently strong, we can use Eq. (1.32) to find the two saddle-node bifurcation points, where the number of solutions changes from one to three and then back from three to one. At these points $d\Omega/d|a|^2 = 0$, yielding a quadratic equation in Ω whose solutions are

$$\Omega_{SN}^{\pm} = \frac{3}{4}|a|^2 \pm \frac{1}{2}\sqrt{\frac{3}{16}\left(3 - \eta^2\right)|a|^4 - \eta|a|^2 - 1}. \tag{1.34}$$

When the two solutions are real, corresponding to the two bifurcation points, a linear stability analysis shows that the upper and lower branches of the response are stable solutions and the middle branch that exists for $\Omega_{SN}^- < \Omega < \Omega_{SN}^+$ is unstable. When the drive amplitude g is reduced, it approaches a critical value g_c where the two bifurcation points merge into an inflection point. At this point both $d\Omega/d|a|^2 = 0$ and $d^2\Omega/(d|a|^2)^2 = 0$, providing two equations for determining the critical condition for the onset of bistability, or the existence of two stable solution branches,

$$|a|_c^2 = \frac{8}{3}\frac{1}{\sqrt{3} - \eta}, \quad \Omega_c = \frac{1}{2\sqrt{3}}\frac{3\sqrt{3} + \eta}{\sqrt{3} - \eta}, \quad g_c^2 = \frac{32}{27}\frac{9 + \eta^2}{\left(\sqrt{3} - \eta\right)^3}. \tag{1.35}$$

For the case without nonlinear damping, $\eta = 0$, the critical values are $|a|_c^2 = (4/3)^{3/2}$ and $\Omega_c = (3/4)^{1/2}$, for which the critical drive amplitude is $g_c = (4/3)^{5/4}$. For $0 < \eta < \sqrt{3}$, the critical driving amplitude g_c that is required for having bistability increases with η, as shown in Fig. 1.4. For $\eta > \sqrt{3}$ the discriminant in Eq. (1.34) is always negative, prohibiting the existence of bistability of solutions.

Nonlinear damping acts to decrease the magnitude of the response when it is appreciable, that is when the drive amplitude is large. It gives rise to an effective damping rate for oscillations with magnitude $|a|$ that is given by $1 + \frac{1}{4}\eta|a|^2$, or in terms of the physical parameters by $\Gamma + \frac{1}{4}\tilde{\eta}\tilde{x}_0^2$. When viewing the response as it is plotted in Fig. 1.3, it is difficult to distinguish between the effects of the two forms of damping. The resonance peaks lie on the same back-bone regardless of the existence of a contribution from nonlinear damping. A more useful scheme for seeing the effect of nonlinear damping is to plot the response amplitude scaled by the drive $|a|/g$, often called the responsivity of the resonator, as shown in Fig. 1.5. Without nonlinear damping all peaks have the same height of 1. With nonlinear damping one clearly sees the decrease in the responsivity as the driving amplitude is increased.

The region of bistability, between the two saddle-node bifurcations (1.34) in the response of the driven Duffing resonator, is a source of a number of interesting dynamical features that are often observed in experiments with MEMS & NEMS resonators [3, 47–49]. Most obvious is the existence of hysteresis in quasistatic sweeps
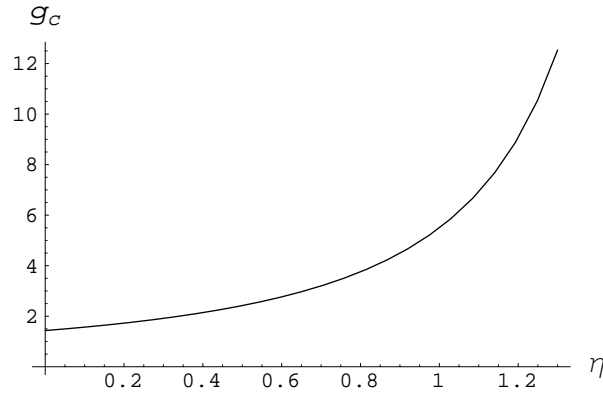
Fig. 1.4 Critical driving amplitude g_c for the onset of bistability in the response of the Duffing resonator as a function of nonlinear damping η, as given by Eq. (1.35). Note that $g_c \rightarrow (4/3)^{5/4} \simeq 1.43$ as $\eta \rightarrow 0$.
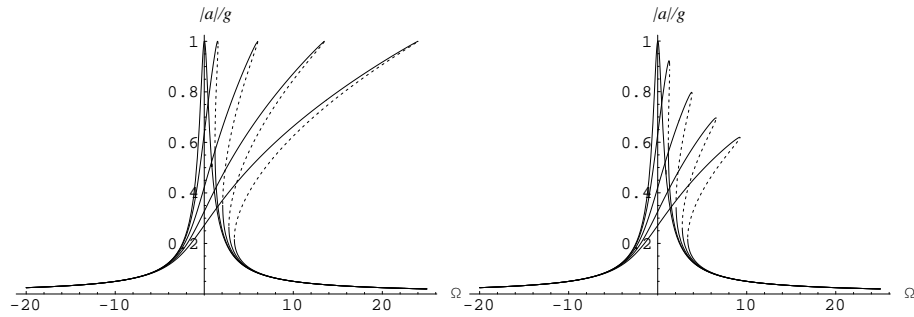

Fig. 1.5 Responsivity $|a|/g$ of the Duffing resonator without non-linear damping (left) and with a small amount of nonlinear damping $\eta = 0.1$ (right), for different values of the driving amplitude g. Viewing the response in this way suggests an experimental scheme by which one could determine the importance of nonlinear damping and extract its magnitude.

of either driving frequency or driving amplitude, which is readily observed in experiments. For example, if we start below resonance and sweep the frequency upwards along one of the constant drive-amplitude curves shown in Fig. 1.3, the response will gradually increase climbing up on the curve until it reaches the upper saddle-node bifurcation $\Omega_{SN}^{+}(g)$ when it will abruptly drop down to the lower stable solution branch, and continue toward lower response amplitudes to the right of the resonance. Upon switching the direction of the quasistatic sweep, the response amplitude will gradually increase until it reaches the lower saddle-node bifurcation $\Omega_{SN}^{-}(g)$ where it will abruptly jump up to the upper stable solution branch, from there on gradually following it downwards towards lower frequencies with diminishing response amplitude.

Another interesting aspect involves the notion of basins of attraction. If we fix the values of the driving amplitude and frequency, then depending on its initial conditions, the driven damped Duffing resonator will deterministically approach one of the two possible solutions. One can then map out the regions of the phase-space of initial conditions into the two so-called basins of attraction of the two possible stable solutions, where the unstable solution lies along the separatrix—the border line between the two basins of attraction. These basins of attraction were mapped out in a recent experiment using a suspended platinum nanowire by Kozinsky et al. [50]. If one additionally considers the existence of a random noise, which is always the case in real systems, then the separatrix becomes fuzzy, and it is possible to observe thermally activated switching of the resonator between its two possible solutions. What in fact is observed, say in an upward frequency scan, is that the resonator can drop to the small amplitude solution before it actually reaches the upper saddle-node bifurcation $\Omega_{SN}^{+}(g)$, and similarly for the lower bifurcation point. As the noise increases the observed size of the bistability region thus effectively shrinks. This was demonstrated with a doubly-clamped nanomechanical resonator made of aluminum nitride in a recent experiment by Aldridge & Clelend [21]. The existence of the saddle-node bifurcation has also been exploited for applications because at the bifurcation point the response of the resonator can change very dramatically if one changes the drive frequency or any of the resonator's physical parameters that can alter the response curve. This idea has been suggested and also used for signal amplification [26] as well as squeezing of noise [42, 49].

Finally, much effort is invested these days to push experiments with nanomechanical resonators towards the quantum regime. In this context, it has been shown that the bistability region in the response of the driven damped Duffing resonator offers a novel approach for observing the transition from classical to quantum mechanical behavior as the temperature is lowered [51]. The essential idea is that one can find a regime in frequency and temperature where thermal switching between the two basins of attraction is essentially suppressed when the dynamics is classical, whereas if the resonator has already started entering the quantum regime, quantum dynamics allow it to switch between the two basins. Thus, an observation of switching can be used to ascertain whether or not a Duffing resonator is behaving quantum mechanically.

1.2.3
Addition of other nonlinear terms

It is worth taking some time to consider the addition of other nonlinear terms that were not included in our original equation of motion (1.18). Without increasing the order of the nonlinearity, we could still add quadratic symmetry-breaking terms of the form x^2, $x\dot{x}$, and $\dot{x}^2$, as well as additional cubic damping terms of the form $\dot{x}^3$, and $x\dot{x}^2$. Such terms may appear naturally in actual physical situations, like the examples discussed in §1.1.2. For the reader who is anxious to skip on to the next section on parametrically-driven Duffing resonators, we state at the outset that the addition of

such terms does not alter the response curves that we described in the previous section in any fundamental way. They merely conspire to renormalize the effective values of the coefficients used in the original equation of motion. Thus, without any particular model at hand, it is difficult to discern the existence of such terms in the equation.

Consider then an equation like (1.18), but with all these additional terms

$$m\frac{d^2\tilde{x}}{d\tilde{t}^2} + \Gamma\frac{d\tilde{x}}{d\tilde{t}} + m\omega_0^2\tilde{x} + \tilde{\beta}\tilde{x}^2 + \tilde{\mu}\tilde{x}\frac{d\tilde{x}}{d\tilde{t}} + \tilde{\rho}\left(\frac{d\tilde{x}}{d\tilde{t}}\right)^2$$

$$+ \tilde{\alpha}\tilde{x}^3 + \tilde{\eta}\tilde{x}^2\frac{d\tilde{x}}{d\tilde{t}} + \tilde{v}\tilde{x}\left(\frac{d\tilde{x}}{d\tilde{t}}\right)^2 + \tilde{\zeta}\left(\frac{d\tilde{x}}{d\tilde{t}}\right)^3 = \tilde{G}\cos\tilde{\omega}\tilde{t}, \quad (1.36)$$

and perform the same scaling as in Eq. (1.20) for the additional parameters,

$$\beta = \frac{\tilde{\beta}}{\omega_0\sqrt{m\tilde{\alpha}}}; \quad \mu = \frac{\tilde{\mu}}{\sqrt{m\tilde{\alpha}}}; \quad \rho = \frac{\tilde{\rho}\omega_0}{\sqrt{m\tilde{\alpha}}}; \quad v = \frac{\tilde{v}\omega_0^2}{\tilde{\alpha}}; \quad \zeta = \frac{\tilde{\zeta}\omega_0^3}{\tilde{\alpha}}. \quad (1.37)$$

This yields, after performing the same scaling as before with $\epsilon = Q^{-1}$, a scaled equation of motion with all the additional nonlinearities,

$$\ddot{x} + \epsilon\dot{x} + x + \beta x^2 + \mu x\dot{x} + \rho\dot{x}^2 + x^3 + \eta x^2\dot{x} + v x\dot{x}^2 + \zeta\dot{x}^3 = \epsilon^{3/2}g\cos\omega t, \quad (1.38)$$

The important difference between this equation and the one we solved earlier (1.21) is that with the same scaling of x with $\sqrt{\epsilon}$ as before we now have terms on the order of ϵ. We therefore need to slightly change our trial expansion to contain such terms as well,

$$x(t) = \sqrt{\epsilon}x_0(t, T) + \epsilon x_{1/2}(t, T) + \epsilon^{3/2}x_1(t, T) + \dots, \quad (1.39)$$

with $x_0 = \frac{1}{2}\left[A(T)e^{it} + c.c.\right]$ as before.

We begin by collecting all terms on the order of ϵ, arriving at

$$\ddot{x}_{1/2} + x_{1/2} = -\frac{1}{2}(\beta + \rho)|A|^2 - \frac{1}{4}\left[(\beta - \rho + i\mu)A^2e^{2it} + c.c.\right]. \quad (1.40)$$

This equation for the first correction $x_{1/2}(t)$ contains no secular terms and therefore can be solved immediately to give

$$x_{1/2}(t) = -\frac{1}{2}(\beta + \rho)|A|^2 + \frac{1}{12}\left[(\beta - \rho + i\mu)A^2e^{2it} + c.c.\right]. \quad (1.41)$$

We substitute this solution into the ansatz (1.39) and back into the equation of motion (1.38), and proceed to collecting terms on the order of $\epsilon^{3/2}$. We find a number of additional terms at this order that did not appear earlier on the right-hand side of Eq. (1.25) for the correction $x_1(t)$,

$$-2\beta x_0 x_{1/2} - \mu\left(x_0\dot{x}_{1/2} + \dot{x}_0 x_{1/2}\right) - 2\rho\dot{x}_0\dot{x}_{1/2} - v x_0\dot{x}_0^2 - \zeta\dot{x}_0^3$$

$$= \left\{\left[\frac{5}{12}\beta(\beta + \rho) + \frac{1}{6}\rho^2 + \frac{1}{24}\mu^2 - \frac{1}{8}v\right] + i\left[\frac{1}{8}\mu(\beta + \rho) - \frac{3}{8}\zeta\right]\right\}|A|^2Ae^{it}$$

$$+ \text{nonsecular terms.}$$

$$(1.42)$$

After adding the additional secular terms, we obtain a modified equation for the slowly varying amplitude $A(T)$,

$$
\frac{dA}{dT} = -\frac{1}{2}A + i\frac{3}{8}\left(1 - \frac{10}{9}\beta\,(\beta + \rho) - \frac{4}{9}\rho^2 - \frac{1}{9}\mu^2 + \frac{1}{3}\nu\right)|A|^2 A
$$
$$
\quad - \frac{1}{8}\left(\eta - \mu\,(\beta + \rho) + 3\zeta\right)|A|^2 A - i\frac{g}{2}e^{i\Omega T} \tag{1.43}
$$
$$
\equiv -\frac{1}{2}A + i\frac{3}{8}\alpha_{eff}|A|^2 A - \frac{1}{8}\eta_{eff}|A|^2 A - i\frac{g}{2}e^{i\Omega T}.
$$

We find that the equation is formally identical to the one we had earlier (1.26) before adding the extra nonlinear terms. The response curves and the discussion of the previous section therefore still apply after taking into account all the quadratic and cubic nonlinear terms. All these terms combine together in a particular way giving rise to the two effective cubic parameters, defined in (1.43). This, in fact, allows one some flexibility in tuning the nonlinearities of a Duffing resonator in real experimental situations. For example, Kozinsky et al. [52] use this flexibility to tune the effective Duffing parameter α_{eff} using an external electrostatic potential, as described in § 1.1.3 and shown in Fig. 1.1, thus affecting both the quadratic parameter $\tilde{\beta}$ and the cubic parameter $\tilde{\alpha}$ in the physical equation of motion (1.36). Note that due to the different signs of the various contributions to the effective nonlinear parameters, one could actually cause the cubic terms to vanish, altering the response in a fundamental way.

1.3
Parametric excitation of a damped Duffing resonator

Parametric excitation offers an alternative approach for actuating MEMS or NEMS resonators. Instead of applying an external force that acts directly on the resonator, one modulates one (or more) of its physical parameters as a function of time, which in turn modulates the normal frequency of the resonator. This is what happens on a swing, where the up-and-down motion of the center of mass of the swinging child effectively changes the length of the swing, thereby modulating its natural frequency. The most effective way to swing is to move the center of mass up-and-down twice in every period of oscillation, but one can also swing by moving up-and-down at slower rates, namely once every n^{th} multiple of half a period, for any integer n. Let H be the relative amplitude by which the normal frequency is modulated, and ω_P be the frequency of the modulation, often called the pump frequency. One can show [53] that there is a sequence of tongue shaped regions in the $H - \omega_P$ plane where the smallest fluctuations away from the quiescent state of the swing, or any other parametrically-excited resonator [15], are exponentially amplified. This happens when the amplitude of the modulation H is sufficiently strong to overcome the effect of damping. The
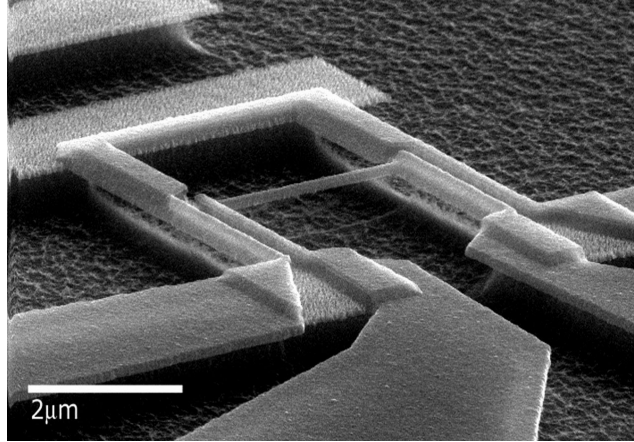
Fig. 1.6 A configuration that uses electromotive actuation to perform parametric excitation of a doubly clamped beam—the central segment of the H-shaped device. A static magnetic field runs normal to the plane of the device. A metallic wire that runs along the external suspended segments of the H-device carries alternating current in opposite directions, thus applying opposite Lorentz forces that induce a time-varying compression of the central segment. This modulates the tension in the central segment, thus varying its normal frequency. This configuration was recently used by Karabalin et. al to demonstrate parametric amplification of a signal running along the central beam through a separate electric circuit. Image courtesy of Michael Roukes.

threshold for the nth instability tongue scales as $(Q^{-1})^{1/n}$. Above this threshold, the amplitude of the motion grows until it is saturated by nonlinear effects. We shall describe the nature of these oscillations for driving above threshold later on, both for the first ($n = 1$) and the second ($n = 2$) instability tongues, but first we shall consider the dynamics when the driving amplitude is just below threshold, as it also offers interesting behavior, and a possibility for novel applications such as parametric amplification [23, 24, 54] and noise squeezing [23].

There are a number of actual schemes for the realization of parametric excitation in MEMS & NEMS devices. The simplest, and probably the one most commonly used in the micron scale, is to use an external electrode that can induce an external potential that, if modulated in time, changes the effective spring constant of the resonator [15, 18, 19, 31, 55, 56]. Based on our treatment of this situation in § 1.1.3, this method is likely to modulate all the coefficients in the potential felt by the resonator, thus modulating, for example, also the Duffing parameter α. Similarly, one may devise configurations in which an external electrode deflects a doubly-clamped beam from its equilibrium, thereby inducing extra tension within the beam itself, as described in § 1.1.4, that can be modulated in time. Alternatively, one may generate motion in the clamps holding a doubly-clamped beam by its ends, as shown for example in Fig. 1.6,

thus inducing in it a time-varying tension, which is likely to affect the other physical parameters to a lesser extent. These methods allow one to modulate the tension in the beam directly and thus modulate its normal frequency. More recently, Masmanidis et al. [57] developed layered piezoelectric NEMS structures whose tension can be fine tuned in doubly-clamped configurations, thus enabling fine control of the normal frequency of the beam with a simple turn of a knob.

Only a minor change is required in our equation of the driven damped Duffing resonator to accommodate this new situation, namely the addition of a modulation of the linear spring constant. Beginning with the scaled form of the Duffing equation (1.19) we obtain

$$\ddot{x} + Q^{-1}\dot{x} + [1 + H\cos\omega_P t]\, x + x^3 + \eta x^2\dot{x} = G\cos\left(\omega_D t + \phi_g\right), \tag{1.44}$$

where the scaling is the same as before, and we shall again use the damping Q^{-1} to define the small expansion parameter ϵ. The term proportional to H on the left hand side is the external drive that modulates the spring constant, giving a term that is proportional to the displacement x as well as to the strength of the drive—this is the parametric drive. We consider first the largest excitation effect that occurs when the pump frequency is close to twice the resonant frequency of the resonator. This is the region in the $H - \omega_P$ plane that we termed the first instability tongue. We therefore take the pump frequency to be an amount $\epsilon\Omega_P$ away from twice the resonant frequency, and take the drive amplitude to scale as the damping, i.e. we set $H = \epsilon h$. The term on the right hand side is a direct additive drive or signal, with amplitude scaled as in the discussion of the Duffing equation. The frequency of the drive is an amount $\varepsilon\Omega_D$ away from the resonator frequency which has been scaled to 1.

The scaled equation of motion that we now treat in detail is therefore

$$\ddot{x} + \epsilon\dot{x} + \left(1 + \epsilon h\cos\left[(2 + \epsilon\Omega_P)\, t\right]\right) x + x^3 + \eta x^2\dot{x} = \epsilon^{3/2}|g|\cos\left[(1 + \epsilon\Omega_D)\, t + \phi_g\right], \tag{1.45}$$

where we now use $g = |g|e^{i\phi_g}$ to denote a complex drive amplitude. We follow the same scheme of secular perturbation theory as in §1.2.2, using a trial solution in the form of Eq. (1.22) and proceeding as before. The new secular term, appearing on the right-hand side of Eq. (1.25), arising from the parametric drive is

$$-\frac{1}{4}hA^* e^{i\Omega_P T} e^{it}. \tag{1.46}$$

This gives the equation for the slowly varying amplitude,

$$\frac{dA}{dT} + \frac{1}{2}A - i\frac{h}{4}A^* e^{i\Omega_P T} - i\frac{3}{8}|A|^2 A + \frac{\eta}{8}|A|^2 A = -i\frac{g}{2}e^{i\Omega_D T}. \tag{1.47}$$

1.3.1
Driving below threshold: Amplification and noise squeezing

We first study the amplitude of the response of a parametrically-pumped Duffing resonator to an external direct drive $g \neq 0$. We will see that the characteristic behavior changes from amplification of an applied signal to oscillations, even in the absence of a signal, at a critical value of $h = h_c = 2$. It is therefore convenient to introduce a reduced parametric drive $\bar{h} = h/h_c = h/2$ which plays the role of a bifurcation parameter with a critical value of 1. We begin by assuming that the drive is small enough so that the magnitude of the response remains small and the nonlinear terms in Eq. (1.47) can be neglected. This gives the linear equation

$$\frac{dA}{dT} + \frac{1}{2}A - i\frac{\bar{h}}{2}A^*e^{i\Omega_P T} = -i\frac{g}{2}e^{i\Omega_D T}. \tag{1.48}$$

In general, at long times after transients have died out, the solution will take the form

$$A = a'e^{i\Omega_D T} + b'e^{i(\Omega_P - \Omega_D)T} \tag{1.49}$$

with a', b' complex constants.

We first consider the degenerate case where the pump frequency is tuned to be always twice the signal frequency. In this case $\Omega_P = 2\Omega_D$ and the long time solution is

$$A = ae^{i\Omega_D T} \tag{1.50}$$

with a a time independent complex amplitude. Substituting this into Eq. (1.48) gives

$$(2\Omega_D - i)a - \bar{h}a^* = -g. \tag{1.51}$$

Equation (1.51) is easily solved. If we first look on resonance, $\Omega_D = 0$ we find

$$a = e^{i\pi/4}\left[\frac{\cos(\phi_g + \pi/4)}{(1-\bar{h})} + i\frac{\sin(\phi_g + \pi/4)}{(1+\bar{h})}\right]|g| \tag{1.52}$$

where we we remind the reader that $g = |g|e^{i\phi_g}$ so that ϕ_g measures the phase of the signal relative to the pump. Equation (1.52) shows that on resonance and for $\bar{h} \to 1$ (or $h \to h_c = 2$) there is strongest enhancement of the response for a signal that has a phase $-\pi/4$ relative to the pump. Physically this means that the maximum of the signal occurs a quarter of a pump cycle after a maximum of the pump. (The phase $3\pi/4$ gives the same result: this corresponds to shifting the oscillations by a complete pump period.) The enhancement diverges as $\bar{h} \to 1$, provided that the signal amplitude g is small enough that the enhanced response remains within the linear regime. For a fixed signal amplitude g, the response will become large as $\bar{h} \to 1$ so that the nonlinear terms in Eq. (1.47) must be retained, and the expressions we have derived no longer hold. This situation is discussed in the next section.

On the other hand, for a signal that has a relative phase $\pi/4$ or $5\pi/4$ (the maximum of the signal occurring a quarter of a pump cycle before a maximum of the pump) there

is a weak suppression, by a factor of 2 as $\bar{h} \to 1$. A noise signal on the right-hand side of the equation of motion (1.45) would have both phase components. This leads to the squeezing of the noisy displacement driven by this noise, with the response at phase $-\pi/4$ amplified and the response at phase $\pi/4$ quenched.

The full expression for $\Omega_D \neq 0$ for the amplitude of the response is

$$a = -\left[\frac{2\Omega_D + (i + \bar{h}e^{-2i\phi_g})}{4\Omega_D^2 + (1 - \bar{h}^2)}\right]g. \tag{1.53}$$

For $\bar{h} \to 1$ the response is large when $\Omega_D \ll 1$, that is for frequencies much closer to resonance than the original width of the resonator response. In these limits the first term in the numerator may be neglected unless $\phi_g \simeq \pi/4$. This then gives

$$|a| = \frac{2\left|g\cos(\phi_g + \pi/4)\right|}{4\Omega_D^2 + (1 - \bar{h}^2)}. \tag{1.54}$$

This it not the same as the expression for a resonant response, since the frequency dependence of the amplitude, not amplitude squared, is Lorentzian. However, estimating a quality factor from the width of the sharp peak would give an enhanced quality factor $\propto 1/\sqrt{1 - \bar{h}^2}$, becoming very large as $\bar{h} \to 1$. For the case $\phi_g = \pi/4$ the magnitude of the response is

$$\left|a_{\phi_g=\pi/4}\right| = \frac{\sqrt{4\bar{\Omega}_D^2 + (1 - \bar{h})^2}}{4\bar{\Omega}_D^2 + (1 - \bar{h}^2)}\left|\bar{g}\right|. \tag{1.55}$$

This initially increases as the frequency approaches resonance, but decreases for $\Omega_D \lesssim \sqrt{1 - \bar{h}}$, approaching $|g|/2$ for $\Omega_D \to 0, \bar{h} \to 1$.

For the general or nondegenerate case of $\Omega_P \neq 2\Omega_D$ it is straightforward to repeat the calculation with the ansatz Eq. (1.49). The result is

$$a' = -\frac{2(\Omega_P - \Omega_D) + i}{4\Omega_D(\Omega_P - \Omega_D) - 2i(\Omega_P - 2\Omega_D) + 1 - \bar{h}^2}g. \tag{1.56}$$

Notice that this does not reduce to Eq. (1.53) for $\Omega_P = 2\Omega_D$, since we miss some of the interference terms in the degenerate case if we base the calculation on $\Omega_P \neq 2\Omega_D$. Also, of course, there is no dependence of the magnitude of the response on the phase of the signal ϕ_g, since for different frequencies the phase difference cannot be defined independent of an arbitrary choice of the origin of time. If the pump frequency is maintained fixed at twice the resonator resonance frequency, corresponding to $\Omega_P = 0$, the expression for the amplitude of the response simplifies to

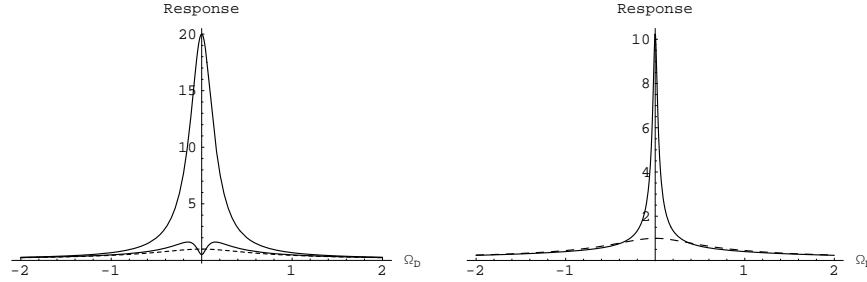$$a' = \frac{2\Omega_D - i}{-4\Omega_D^2 + 4i\Omega_D + 1 - \bar{h}^2}g. \tag{1.57}$$

Fig. 1.7 Response of the parametrically driven resonator as the signal frequency Ω_D varies for pump frequency equal to twice the signal frequency (left) and for the pump frequency fixed at the linear resonance frequency (right), given by equations (1.53) and (1.57) respectively. The dashed curve is the response of the resonator to the same signal without parametric drive. In the left hand figure the upper curve is for the amplified phase $\phi_g = -\pi/4$, and the lower curve is for the phase $\phi_g = \pi/4$, giving squeezing on resonance. In both cases the reduced pump amplitude $\bar{h} = h/h_c$ is 0.95.

Again there is an enhanced response for drive frequencies closer to resonance than the width of the original resonator response. In this region $\Omega_D \ll 1$ so that

$$\left| a' \right| \simeq |g| \frac{1}{\sqrt{(4\Omega_D)^2 + (1 - \bar{h}^2)^2}}. \tag{1.58}$$

This is the usual Lorentzian describing a resonance with a quality factor enhanced by $(1 - \bar{h}^2)^{-1}$, as shown on the right-hand side of Fig. 1.7.

For the resonance condition $\Omega_D = \Omega_P = 0$, corresponding to a pump frequency twice the resonance frequency of the device, and a signal at this resonant frequency, the response amplitude in the linear approximation diverges as the pump amplitude approaches the critical value $h_c = 2$. This is the signature of a linear instability to self sustained oscillations in the absence of any drive. We analyze this parametric instability in the next section.

1.3.2
Linear instability

The divergence of the response as $\bar{h}$ approaches unity from below corresponding to $h \to 2$, suggests a linear instability for $h > 2$, or $QH > 2$ in the original units. We can see this directly from Eq. (1.47) setting $g = 0$ but still ignoring the nonlinear terms, to give the linear equation

$$\frac{dA}{dT} + \frac{1}{2}A = i\frac{h}{4}A^* e^{i\Omega_P T}. \tag{1.59}$$

We seek a solution of the form

$$A = |a| e^{i\phi} e^{\sigma T} e^{i(\Omega_P/2)T} \tag{1.60}$$

with a real σ giving exponential growth or decay. Substituting into Eq. (1.59) gives

$$\sigma = \frac{-1 \pm \sqrt{(h/2)^2 - \Omega_P^2}}{2}, \tag{1.61}$$

$$\phi = \pm \left[\frac{\pi}{4} - \frac{1}{2} \arcsin\left(\frac{2\Omega_P}{h} \right) \right] \tag{1.62}$$

where we take the value of arcsin between 0 and $\pi/2$ and the plus and minus signs in the two equations go together. Note that these expressions apply for $h/2 > \Omega_P$; for $h/2 < \Omega_P$ the value of σ is complex. For pumping at twice the resonance frequency $\Omega_P = 0$, one phase of oscillation $\phi = \frac{\pi}{4}$ has a reduced damping, with $\sigma = -(1/2 - h/4)$ for $h < 2$, and an instability, $\sigma = (h/4 - 1/2) > 0$ signaling exponential growth, for $h > 2$. The other phase of oscillation $\phi = -\frac{\pi}{4}$ has an increased damping, with $\sigma = -(1/2 + h/4)$. The general condition for instability is

$$h > 2\sqrt{1 + \Omega_P^2}, \tag{1.63}$$

showing an increase of the threshold for nonzero frequency detuning $\Omega_P \neq 0\Omega_P$, as shown in Fig. 1.8. The linear instability that occurs for positive σ gives exponentially growing solutions that eventually saturate due to nonlinearity.

1.3.3
Nonlinear behavior near threshold

Nonlinear effects may also be important below the threshold of the parametric instability in the presence of a periodic signal or noise. As we have seen, in the linear approximation, the gain below threshold diverges in the linear approximation as $h \to h_c$. This is unphysical, and for a given signal or noise strength there is some h close enough to h_c where nonlinear saturation of the gain will become important. This will give a smooth behavior of the response of the driven system as h passes through h_c into the unstable regime. We first analyze the effects of nonlinearity near the threshold of the instability, and calculate the smooth behavior as h passes through h_c in the presence of an applied signal. In the following section we study the effects of nonlinearity on the self-sustained oscillations above threshold with more generality.

We take h to be close to h_c, and we take the signal to be small. This introduces a second level of "smallness". We have already assumed that the damping is small and that the deviation of the pump frequency from resonance is small. This means that the critical parametric drive H_c is also small. We now assume that $|H - H_c|$ is small compared with H_c, or equivalently in scaled units that $|h - h_c|$ is small compared with h_c, and introduce the perturbation parameter δ to implement this, i.e., we assume that

$$\delta = \frac{h - h_c}{h_c} \ll 1. \tag{1.64}$$

We now use the same type of secular perturbation theory as the method leading to Eq. (1.47) to develop the expansion in δ. For simplicity we will develop the theory
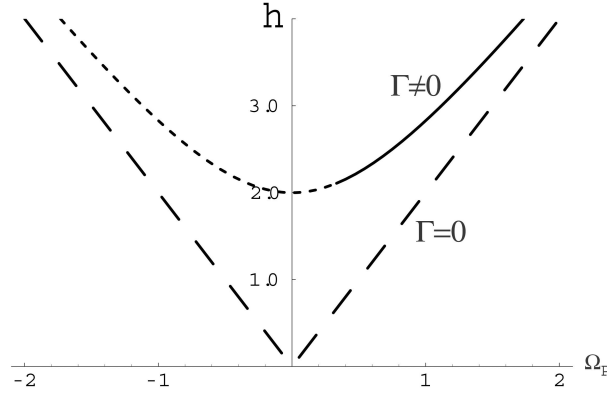
Fig. 1.8 The first instability tongue of the parametrically-driven Duffing resonator—the threshold for instability—plotted in the (Ω_P, h) plane. The lower, long-dashed curve shows the threshold without any linear damping ($\Gamma = 0$), which is zero on resonance. The upper curve shows the threshold with linear damping ($\Gamma \neq 0$). The threshold on resonance ($\Omega_P = 0$) is $h = 2$. The solid and short-dashed regions of the upper curve indicate the so-called subcritical and supercritical branches of the instability, respectively, as discussed in section 1.3.4. On the subcritical branch ($\Omega_P > 4\eta/3$) there will be hysteresis as h is varied, and on the supercritical branch ($\Omega_P < 4\eta/3$) there will not be any hysteresis.

for the most interesting case of resonant pump and signal frequencies $\Omega_P = \Omega_D = 0$. The critical value of h is then $h_c = 2$, and the solution to Eq. (1.47) that becomes marginally stable at this value is

$$A = be^{i\pi/4}, \tag{1.65}$$

with b a real constant.

For h near h_c we make the ansatz for the solution

$$A = \delta^{1/2} b_0(\tau) e^{i\pi/4} + \delta^{3/2} b_1(\tau) + \cdots . \tag{1.66}$$

with b_0 a real function of $\tau = \delta T$, a new, even slower, time scale that sets the scale for the time variation of the real amplitude b_0 near threshold. We must also assume the signal amplitude is very small, $g = \delta^{3/2}\hat{g}$, altogether having $G = (\epsilon\delta)^{3/2}\hat{g}$. Substituting Eq. (1.66) into Eq. (1.47) and collecting terms at $O(\delta^{3/2})$ yields

$$\frac{1}{2}(b_1 - b_1^*) = -\frac{\hat{g}}{2}e^{i\pi/4} - \frac{db_0}{d\tau} + \frac{1}{2}b_0 + i\frac{3}{8}b_0^3 - \frac{\eta}{8}b_0^3. \tag{1.67}$$

The left-hand side of this equation is necessarily imaginary, so in order to have a solution for b_1, so that the perturbation expansion is valid, the real part of the right-hand side must be zero. This is the solvability condition for the secular perturbation

theory. This gives

$$\frac{db_0}{d\tau} = \frac{1}{2}b_0 - \frac{\eta}{8}b_0^3 - \frac{|\hat{g}|}{2}\cos(\phi_g + \pi/4). \tag{1.68}$$

It is more informative to write this equation in terms of the variables without the δ scaling. Introducing the "unscaled" amplitude $b = \delta^{1/2}b_0$, generalizing Eq. (1.65) so that

$$A = be^{i\pi/4} + O(\delta^{3/2}), \tag{1.69}$$

we can write the equation as

$$\frac{db}{dT} = \frac{1}{2}\frac{h - h_c}{h_c}b - \frac{\eta}{8}b^3 - \frac{|g|}{2}\cos(\phi_g + \pi/4). \tag{1.70}$$

Equation (1.70) can be used to investigate many phenomena, such as transients above threshold, and how the amplitude of the response to a signal varies as h passes through the instability threshold. The unphysical divergence of the response to a small signal as $h \to h_c$ from below is now eliminated. For example, exactly at threshold $h = h_c$ we have

$$|b| = \left(\frac{4}{\eta}\left|g\cos(\phi_g + \pi/4)\right|\right)^{1/3}, \tag{1.71}$$

giving a finite response, but one proportional to $|g|^{1/3}$ rather than to $|g|$. The gain $|b/g|$ scales as $|g|^{-2/3}$ for $h = h_c$, and gets smaller as the signal gets larger, as shown in Fig. 1.9. Note that the physical origin of the saturation at the lowest order of perturbation theory is nonlinear damping. Without nonlinear damping the response amplitude (1.71) still diverges. With linear damping being also small, one would need to go to higher orders of perturbation theory to find a different physical mechanism that can provide this kind of saturation. The response to noise can also be investigated, by replacing the $|g|\cos(\phi_g + \pi/4)$ drive by a noise function. Equation (1.70), and the noisy version, appear in many contexts of phase transitions and bifurcations, and so solutions are readily found in the literature [46].

1.3.4
Nonlinear saturation above threshold

The linear instability leads to exponential growth of the amplitude, regardless of the signal, and we need to turn to the full nonlinear equation (1.47) with $g = 0$ to understand the saturation of this amplitude. Ignoring initial transients, and assuming that the nonlinear terms in the equation are sufficient to saturate the growth of the instability, we try a steady-state solution of the form

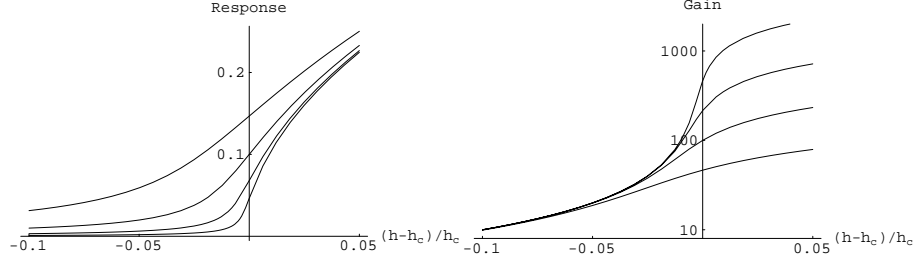$$A(T) = ae^{i\left(\frac{\Omega_P}{2}\right)T}, \tag{1.72}$$

Fig. 1.9 Saturation of the response b (left) and gain $|b/g|$ (right) as the parametric drive h passes through the critical value h_c, for four different signal levels g. The signal levels are $\sqrt{\eta/4}$ times $10^{-2.5}$, 10^{-3}, $10^{-3.5}$, and 10^{-4}, increasing upwards for the response figure, and downwards for the gain figure. The response amplitude is also measured in units of $\sqrt{\eta/4}$. The phase of the signal is $\phi_g = -\pi/4$.

This amplitude a can be any solution of the equation

$$\left[\left(\frac{3}{4}|a|^2 - \Omega_P\right) + i\left(1 + \frac{\eta}{4}|a|^2\right)\right]a = \frac{h}{2}a^*, \tag{1.73}$$

obtained by substituting the steady-state solution (1.72) into the equation (1.47) of the secular terms. We immediately see that having no response ($a = 0$) is always a possible solution regardless of the excitation frequency Ω_P. Expressing $a = |a|e^{i\phi}$ we obtain, after taking the magnitude squared of both sides, the intensity $|a|^2$ of the non-trivial response as all positive roots of the equation

$$\left(\Omega_P - \frac{3}{4}|a|^2\right)^2 + \left(1 + \frac{\eta}{4}|a|^2\right)^2 = \frac{h^2}{4}. \tag{1.74}$$

After having noted that $|a| = 0$ is always a solution, we are left with a quadratic equation for $|a|^2$ and therefore, at most, two additional positive solutions for $|a|$. This has the form of a distorted ellipse in the $(\Omega_P, |a|^2)$ plane, and a parabola in the $(|a|^2, h)$ plane. In addition, we obtain for the relative phase of the response

$$\phi = \frac{i}{2}\ln\frac{a^*}{a} = -\frac{1}{2}\arctan\frac{1 + \frac{\eta}{4}|a|^2}{\frac{3}{4}|a|^2 - \Omega_P}. \tag{1.75}$$

In Figure 1.10 we plot the response intensity $|a|^2$ of a Duffing resonator to parametric excitation as a function of the pump frequency Ω_P, for a fixed scaled drive amplitude $h = 3$. Solid curves indicate stable solutions, and dashed curves are solutions that are unstable to small perturbations. Thin curves show the response without nonlinear damping ($\eta = 0$) which grows indefinitely with frequency Ω_P and is therefore incompatible with experimental observations [15, 19, 58] and the assumptions of our calculation. Again, as we saw for the saturation below threshold, without nonlinear
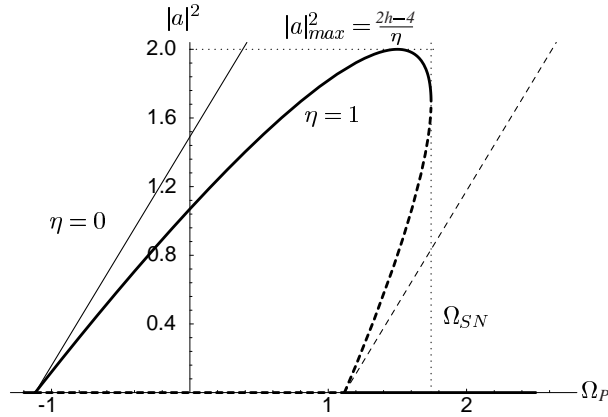
Fig. 1.10 Response intensity $|a|^2$ as a function of the pump frequency Ω_P, for fixed amplitude $h = 3$. Solid curves are stable solutions; dashed curves are unstable solutions. Thin curves show the response without non-linear damping ($\eta = 0$). Thick curves show the response for finite nonlinear damping ($\eta = 1$). Dotted lines indicate the maximal response intensity $|a|^2_{max}$ and the saddle-node frequency Ω_{SN}.
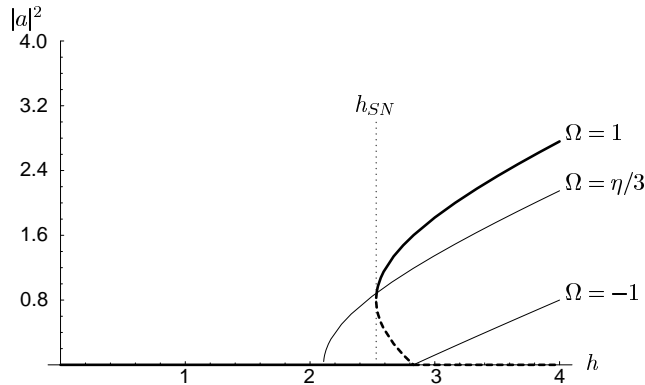

Fig. 1.11 Response intensity $|a|^2$ as a function of the parametric drive amplitude h for fixed frequency Ω_P and finite nonlinear damping ($\eta = 1$). Thick curves show the stable (solid curves) and unstable (dashed curves) response for $\Omega_P = 1$. Thin curves show the stable solutions for $\Omega_P = \eta/3$ and $\Omega_P = -1$, and demonstrate that hysteresis as h is varied is expected only for $\Omega_P > \eta/3$.

damping and with linear damping being small, one would have to go to higher orders of perturbation theory to search for a physical mechanism that could provide saturation. For large linear damping, or small Q, one sees saturation even without nonlinear damping [59]. Thick curves show the response with finite nonlinear damping ($\eta = 1$). With finite η there is a maximum value for the response $|a|^2_{max} = 2(h - 2)/\eta$, and a

maximum frequency,

$$\Omega_{SN} = \frac{h}{2}\sqrt{1 + \left(\frac{3}{\eta}\right)^2} - \frac{3}{\eta}, \tag{1.76}$$

at a saddle-node bifurcation, where the stable and unstable nontrivial solutions meet. For frequencies above Ω_{SN} the only solution is the trivial one $a = 0$. These values are indicated by horizontal and vertical dotted lines in Figure 1.10.

The threshold for the instability of the trivial solution is easily verified by setting $a = 0$ in the expression (1.74) for the nontrivial solution, or by inverting the expression (1.63) for the instability that we obtained in the previous section. As seen in Figure 1.10, for a given h the threshold is situated at $\Omega_P = \pm\sqrt{(h/2)^2 - 1}$. This is the same result calculated in the previous section, where we plotted the threshold tongue in Fig. 1.8, in the (h, Ω_P) plane. Fig. 1.10 is a cut going horizontally through that tongue at a constant drive amplitude $h = 3$.

Like the response of a forced Duffing resonator (1.29), the response of a parametrically excited Duffing resonator also exhibits hysteresis in quasistatic frequency scans. If the frequency Ω_P starts out at negative values and is increased gradually with a fixed amplitude h, the zero response will become unstable as the lower threshold is crossed at $-\sqrt{(h/2)^2 - 1}$, after which the response will gradually increase along the thick solid curve in Fig. 1.10, until Ω_P reaches Ω_{SN} and the response drops abruptly to zero. If the frequency is then decreased gradually, the response will remain zero until Ω_P reaches the upper instability threshold $+\sqrt{(h/2)^2 - 1}$, and the response will jump abruptly to the thick solid curve above, and then gradually decrease to zero along this curve.

Finally, in Fig. 1.11 we plot the response intensity $|a|^2$ of the Duffing resonator as a function of drive amplitude h, for fixed frequency Ω_P and finite nonlinear damping $\eta = 1$. This would correspond to performing a vertical cut through the instability tongue 1.8. Again, solid curves indicate stable solutions, and dashed curves unstable solutions. Thick curves show the response for $\Omega_P = 1$, and thin curves show the response for $\Omega_P = \eta/3$ and $\Omega_P = -1$. The intersection of the trivial and the nontrivial solutions, which corresponds to the instability threshold (1.63), occurs at $h = 2\sqrt{\Omega_P^2 + 1}$. For $\Omega_P < \eta/3$ the nontrivial solution for $|a|^2$ grows continuously for h above threshold and is stable. This is a supercritical bifurcation. On the other hand, for $\Omega_P > \eta/3$ the bifurcation is subcritical—the nontrivial solution grows for h below threshold. This solution is unstable until the curve of $|a|^2$ as a function of h bends around at a saddle-node bifurcation at

$$h_{SN} = \frac{2 + \frac{2\eta}{3}\Omega_P}{\sqrt{1 + \left(\frac{\eta}{3}\right)^2}}, \tag{1.77}$$

where the solution becomes stable and $|a|^2$ is once more an increasing function of h. For amplitudes $h < h_{SN}$ the only solution is the trivial one $a = 0$. Hysteretic behavior

is therefore expected for quasistatic scans of the drive amplitude h only if the fixed frequency $\Omega_P > \eta/3$, as can be inferred from Figure 1.11.

1.3.5
Parametric excitation at the second instability tongue

We wish to examine the second tongue—which is readily accessible in experiments because in this case the pump and the response frequencies are the same—by looking at the response above threshold and highlighting the main changes from the first tongue. We start with the general equation for a parametrically-driven Duffing resonator (1.44), but with no direct drive ($g = 0$), where the parametric excitation is performed around 1 and not around 2. Correspondingly, the scaling of H with respect to ϵ needs to be changed to $H = h\sqrt{\epsilon}$. The technical reason for doing this is that if we naively take $H = h\epsilon$ as before, the parametric driving term does not contribute to the order $\epsilon^{3/2}$ secular term which we use to find the response, and the order $\epsilon^{1/2}$ term in x becomes identically zero. Scaling H in this manner, as we shall immediately see, will introduce a non-secular correction to x at order ϵ, and this correction will contribute to the order $\epsilon^{3/2}$ secular term and will give us the required response. The equation of motion then becomes

$$\ddot{x} + x = -\frac{h\epsilon^{1/2}}{2}\left(e^{i(t+\Omega_P T)} + c.c.\right)x - \epsilon\dot{x} - x^3 - \eta x^2 \dot{x}, \tag{1.78}$$

and we try an expansion of the solution of the form

$$x(t) = \epsilon^{1/2}\frac{1}{2}\left(A(T)e^{it} + c.c.\right) + \epsilon x_{1/2}(t) + \epsilon^{3/2}x_1(t) + \dots \tag{1.79}$$

Substituting this expansion into the equation of motion (1.78) we obtain at order $\epsilon^{1/2}$ the linear equation as usual, and at order ϵ

$$\ddot{x}_{1/2} + x_{1/2} = -\frac{h}{4}\left(Ae^{i\Omega_P T}e^{2it} + A^*e^{i\Omega_P T} + c.c.\right). \tag{1.80}$$

As expected, there is no secular term on the right-hand side, so we can immediately solve for $x_{1/2}$,

$$x_{1/2}(t) = \frac{h}{4}\left(\frac{A}{3}e^{i\Omega_P T}e^{2it} - A^*e^{i\Omega_P T} + c.c.\right) + O(\epsilon). \tag{1.81}$$

Substituting the solution for $x_{1/2}$ into the expansion (1.79), and the expansion back into the equation of motion (1.78), contributes an additional term from the parametric driving which has the form

$$\epsilon^{3/2}\frac{h^2}{8}\left(-\frac{A}{3}e^{i\Omega_P T}e^{2it} + A^*e^{i\Omega_P T} + c.c.\right)\left(e^{i\Omega_P T}e^{it} + c.c.\right)$$
$$= \epsilon^{3/2}\frac{h^2}{8}\left(\frac{2}{3}A + A^*e^{i2\Omega_P T}\right)e^{it} + c.c. + \text{ non secular terms}. \tag{1.82}$$

This gives us the required contribution to the equation for the vanishing secular terms. All other terms remain as they were in Eq. (1.47), so that the new equation for determining $A(T)$ becomes

$$\frac{dA}{dT} + i\frac{h^2}{8}\left(\frac{2}{3}A + A^*e^{i2\Omega_P T}\right) + \frac{1}{2}A - i\frac{3}{8}|A|^2A + \frac{\eta}{8}|A|^2A = 0. \tag{1.83}$$

Again, ignoring initial transients, and assuming that the nonlinear terms in the equation are sufficient to saturate the growth of the instability, we try a steady-state solution, this time of the form

$$A(T) = ae^{i\Omega_P T}. \tag{1.84}$$

The solution to the equation of motion (1.78) is therefore

$$x(t) = \epsilon^{1/2}(ae^{i(1+\epsilon\Omega_P)t} + c.c.) + O(\epsilon), \tag{1.85}$$

where the correction $x_{1/2}$ of order ϵ is given in Eq. (1.81) and, as before, we are not interested in the correction $x_1(t)$ of order $\epsilon^{3/2}$, but rather in the fixed amplitude a of the lowest order term. We substitute the steady-state solution (1.84) into the equation (1.83) of the secular terms and obtain

$$\left[\left(\frac{3}{4}|a|^2 - 2\Omega_P - \frac{h^2}{6}\right) + i\left(1 + \frac{\eta}{4}|a|^2\right)\right]a = \frac{h^2}{4}a^*. \tag{1.86}$$

By taking the magnitude squared of both sides we obtain, in addition to the trivial solution $a = 0$, a non-trivial response given by

$$\left(\frac{3}{4}|a|^2 - 2\Omega_P - \frac{1}{6}h^2\right)^2 + \left(1 + \frac{\eta}{4}|a|^2\right)^2 = \frac{h^4}{16}. \tag{1.87}$$

Fig. 1.12 shows the response intensity $|a|^2$ as a function of the frequency Ω_P, for a fixed drive amplitude of $h = 3$ producing a horizontal cut through the second instability tongue. The solution looks very similar to the response shown in Fig. 1.10 for the first instability tongue, though we should point out two important differences. The first is that the orientation of the ellipse, indicated by the slope of the curves for $\eta = 0$, is different. The slope here is $8/3$ whereas for the first instability tongue the slope is $4/3$. The second is the change in the scaling of h with ϵ, or the inverse quality factor Q^{-1}. The lowest critical drive amplitude for an instability at the second tongue is again on resonance ($\Omega_P = 0$), and its value is again $h = 2$, but now this implies that $H\sqrt{Q} = 2$, or that H scales the square root of the linear damping rate Γ. This is consistent with the well known result (see, for example, [53, § 3]) that the minimal amplitude for the instability of the nth tongue scales as $\Gamma^{1/n}$.
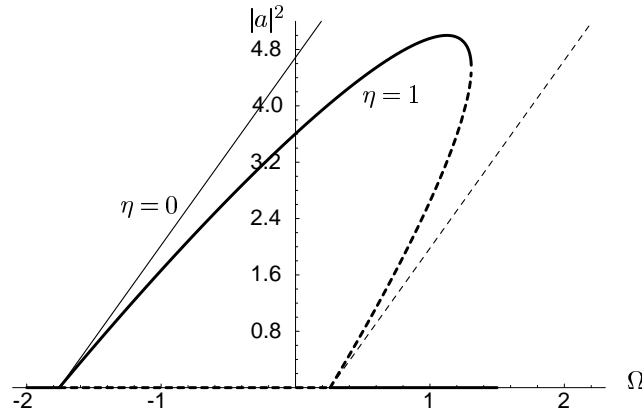
Fig. 1.12 Response intensity $|a|^2$ of a parametrically-driven Duffing resonator as a function of the pump frequency Ω_P, for a fixed amplitude $h = 3$ in the second instability tongue. Solid curves are stable solutions; dashed curves are unstable solutions. Thin curves show the response without non-linear damping ($\eta = 0$). Thick curves show the response for finite nonlinear damping ($\eta = 1$).

1.4
Parametric excitation of arrays of coupled Duffing resonators

The last two sections of this review describe theoretical work that was motivated directly by the experimental work of Buks and Roukes [37], who fabricated an array of non-linear micromechanical doubly-clamped gold beams, and excited them parametrically by modulating the strength of an externally-controlled electrostatic coupling between neighboring beams. The Buks and Roukes experiment was modeled by Lifshitz and Cross [60, henceforth LC] using a set of coupled nonlinear equations of motion. They used secular perturbation theory—as we have described so far for a system with just a single degree of freedom—to convert these equations of motion into a set of coupled nonlinear algebraic equations for the normal mode amplitudes of the system, enabling them to obtain exact results for small arrays, but only a qualitative understanding of the dynamics of large arrays. We shall review these results in this section.

In order to obtain analytical results for large arrays, Bromberg, Cross, and Lifshitz [61, henceforth BCL] studied the same system of equations, approaching it from the continuous limit of infinitely-many degrees of freedom, and obtaining a description of the slow spatiotemporal dynamics of the array of resonators in terms of an amplitude equation. BCL showed that this amplitude equation could predict the initial mode that develops at the onset of parametric oscillations as the driving amplitude is gradually increased from zero, as well as a sequence of subsequent transitions to other single-mode oscillations. We shall review these results in section 1.5. Kenig, Lifshitz, and Cross [62] are currently extending the investigation of the amplitude equation to more general questions such as pattern selection when many patterns or solutions are

simultaneously stable, as well as other experimentally-relevant question such as the response of the system of coupled resonators to time dependent sweeps of the control parameters, rather than quasistatic sweeps like the ones we have been discussing here.

1.4.1
Modeling an array of coupled Duffing resonators

LC modeled the array of coupled nonlinear resonators that was studied by Buks and Roukes using a set of coupled equations of motion (EOM) of the form

$$
\ddot{u}_n + u_n + u_n^3 - \frac{1}{2} Q^{-1} (\dot{u}_{n+1} - 2\dot{u}_n + \dot{u}_{n-1})
$$
$$
+ \frac{1}{2} \left(D + H \cos \omega_p t \right) (u_{n+1} - 2u_n + u_{n-1})
$$
$$
- \frac{1}{2} \eta [(u_{n+1} - u_n)^2 (\dot{u}_{n+1} - \dot{u}_n) - (u_n - u_{n-1})^2 (\dot{u}_n - \dot{u}_{n-1})] = 0, \qquad (1.88)
$$

where $u_n(t)$ describes the deviation of the nth resonator from its equilibrium, with $n = 1 \ldots N$, and fixed boundary conditions $u_0 = u_{N+1} = 0$. Detailed arguments for the choice of terms introduced into the equations of motion are discussed in Ref. [60]. The terms include an elastic restoring force with both linear and cubic contributions (whose coefficients are both scaled to 1 as in our discussion of the single degree of freedom), a dc electrostatic nearest-neighbor coupling term with a small ac component responsible for the parametric excitation (with coefficients D and H respectively), and linear as well as cubic nonlinear dissipation terms. Both dissipation terms are assumed to depend on the difference of the displacements of nearest neighbors.

We consider here a slightly simpler and more general model for an array of coupled resonators to illustrate the approach. Motivated by the geometry of most experimental NEMS systems we suppose a line of identical resonators, although the generalization to two or three dimensions is straightforward. The simplest model is to take the equation of motion of each resonator to be as in (1.44) with the addition of a coupling term to its two neighbors. A simple choice would be to assume this coupling does not introduce additional dissipation, which we describe as reactive coupling. Elastic and electrostatic coupling might be predominantly of this type. After the usual scaling, the equations of motions would take the form

$$
\ddot{u}_n + Q^{-1} \dot{u}_n + u_n^3 + (1 + H \cos \omega_P t) u_n + \eta u_n^2 \dot{u}_n + \frac{1}{2} D(u_{n+1} - 2u_n + u_{n-1}) = 0
$$
$$
(1.89)
$$

where we do not take into account any direct drive for the purposes of the present section.

The equations of motion for particular experimental implementations might have different terms, although we expect all will have linear and nonlinear damping, linear coupling, and parametric drive. For example, to model the experimental setup of Buks

and Roukes [37], LC supposed that both linear and nonlinear dissipation terms involved the difference of neighboring displacements, i.e., the terms involving $\dot{u}_n$ in our equations of motion here (1.89) are replaced with terms involving $u_{n+1} - u_n$ in the equations of motion (1.88), used by LC. This was to describe the physics of electric current damping, with the currents driven by the varying capacitance between neighboring resonators depending on the change in separation and the fixed DC voltage. This effect seemed to be the dominant component of the dissipation in the Buks and Roukes experiments. Similarly the parametric drive $H \cos \omega_P t$ multiplied $(u_{n+1} - 2u_n + u_{n-1})$ in the equations of LC rather than u_n here, since the voltage between adjacent resonators was the quantity modulated, changing the electrostatic component of the spring constant. In more recent implementations [57], the electric current damping has been reduced, and the parametric drive is applied piezoelectrically directly to each resonator, so that the simpler equation (1.89) applies. The method of attack is the same in any case. We will illustrate the approach on the simpler equation, and refer the reader to LC for that more complicated model. An additional complication in a realistic model may be that the coupling is longer range than nearest neighbor. For example both electrostatic coupling and elastic coupling through the supports would have longer range components. The general method is the same for these additional effects, and the reader should be able to apply the approach to the model for their particular experimental implementation.

1.4.2
Calculating the response of an array

We calculate the response of the array to parametric excitation, again using secular perturbation theory. We suppose Q is large and take $\epsilon = Q^{-1}$ as the small expansion parameter. As in § 1.3 we take $H = \epsilon h$ but we also take $D = \epsilon d$ so that the width of the frequency band of eigenmodes is also small. This is not quite how LC treated the coupling, but we think the present approach is clearer, and it is equivalent up to the order of the expansion in ϵ that we require. We thank Eyal Kenig for pointing out this simplification. The equations of motion are now

$$
\ddot{u}_n + \epsilon \dot{u}_n + u_n^3 + (1 + \epsilon h \cos[(2 + \epsilon \Omega_P)t])u_n + \eta u_n^2 \dot{u}_n
$$
$$
+ \frac{1}{2}\epsilon d(u_{n+1} - 2u_n + u_{n-1}) = 0, \qquad n = 1 \ldots N. \tag{1.90}
$$

We expand $u_n(t)$ as a sum of standing wave modes with slowly varying amplitudes. The nature of the standing wave modes will depend on the conditions at the end of the line of resonators. In the experiments of Buks and Roukes there where N mobile beams with a number of identical immobilized beams at each end. These conditions can be implemented in a nearest neighbor model by taking two additional resonators, u_0 and u_{N+1} and assuming

$$
u_0 = u_{N+1} = 0. \tag{1.91}
$$

The standing wave modes are then

$$u_n = \sin(nq_m) \qquad \text{with} \qquad q_m = \frac{m\pi}{N+1}, \ m = 1\ldots N. \tag{1.92}$$

On the other hand for a line of N resonators with free ends there is no force from outside the line. For the nearest neighbor model this can be imposed again by taking two additional resonators, but now with the conditions

$$u_0 = u_1; \qquad u_N = u_{N+1}. \tag{1.93}$$

The standing wave modes are now

$$u_n = \cos[(n - \frac{1}{2})q_m] \qquad \text{with} \qquad q_m = \frac{m\pi}{N}, \ m = 0\ldots N - 1. \tag{1.94}$$

For our illustration we will take Eqs. (1.91,1.92). Thus we write

$$u_n(t) = \epsilon^{1/2} \frac{1}{2} \sum_{m=1}^{N} \left(A_m(T) \sin(nq_m) e^{it} + c.c. \right) + \epsilon^{3/2} u_n^{(1)}(t) + \ldots, \quad n = 1\ldots N. \tag{1.95}$$

with q_m as in Eq. (1.92).

We substitute the trial solution (1.95) into the EOM term by term. Up to order $\epsilon^{3/2}$ we have:

$$\ddot{u}_n = \epsilon^{1/2} \frac{1}{2} \sum_m \sin(nq_m) \left([-A_m + 2i\epsilon A'_m] e^{it} + c.c. \right) + \epsilon^{3/2} \ddot{u}_n^{(1)}(t) + \ldots, \tag{1.96a}$$

$$\epsilon \dot{u}_n = \epsilon^{3/2} \frac{1}{2} \sum_m \sin(nq_m) \left(i A_m e^{it} + c.c. \right) + \ldots, \tag{1.96b}$$

$$\frac{1}{2}\epsilon d(u_{n+1} - 2u_n + u_{n-1}) = -\epsilon^{3/2} \frac{d}{2} \sum_m 2\sin^2\left(\frac{q_m}{2}\right) \sin(nq_m) \left(A_m e^{it} + c.c. \right) + \ldots \tag{1.96c}$$

$$u_n^3 = \epsilon^{3/2} \frac{1}{8} \sum_{j,k,l} \sin(nq_j) \sin(nq_k) \sin(nq_l)$$
$$\times \left(A_j e^{it} + c.c. \right) \left(A_k e^{it} + c.c. \right) \left(A_l e^{it} + c.c. \right)$$
$$= \epsilon^{3/2} \frac{1}{32} \sum_{j,k,l} \{\sin[n(-q_j + q_k + q_l)] + \sin[n(q_j - q_k + q_l)]$$
$$+ \sin[n(q_j + q_k - q_l)] - \sin[n(q_j + q_k + q_l)]\}$$
$$\times \left\{ A_j A_k A_l e^{3it} + 3 A_j A_k A_l^* e^{it} + c.c. \right\}, \tag{1.96d}$$

and

$$\eta u_n{}^2 \dot{u}_n = \epsilon^{3/2} \frac{\eta}{32} \sum_{j,k,l} \left\{ \sin[n(-q_j + q_k + q_l)] + \sin[n(q_j - q_k + q_l)] \right.$$
$$+ \sin[n(q_j + q_k - q_l)] - \sin[n(q_j + q_k + q_l)] \right\}$$
$$\times \left(A_j e^{it} + c.c. \right) \left(A_k e^{it} + c.c. \right) \left(i A_l e^{it} + c.c. \right). \qquad (1.96e)$$

The order $\epsilon^{1/2}$ terms cancel, and at order $\epsilon^{3/2}$ we get N equations of the form

$$\ddot{u}_n^{(1)} + u_n^{(1)} = \sum_m \left(m^{th} \text{ secular term} \right) e^{it} + \text{other terms}, \qquad (1.97)$$

where the left-hand sides are uncoupled linear harmonic resonators, with a frequency unity. On the right-hand sides we have N secular terms which act to drive the resonators $u_n^{(1)}$ at their resonance frequencies. As we did for all the single resonator examples, here too we require that all the secular terms vanish so that the $u_n^{(1)}$ remain finite, and thus obtain equations for the slowly varying amplitudes $A_m(T)$. To extract the equation for the mth amplitude $A_m(T)$ we make use of the orthogonality of the modes, multiplying all the terms by $\sin(nq_m)$ and summing over n. We find that the coefficient of the mth secular term, which is required to vanish, is given by

$$-2i \frac{dA_m}{dT} - i A_m + 2d \sin^2\left(\frac{q_m}{2}\right) A_m - \frac{1}{2} h A_m^* e^{i\Omega_P T}$$
$$- \frac{3 + i\eta}{16} \sum_{j,k,l} A_j A_k A_l^* \Delta_{jkl;m}^{(1)} = 0, \quad (1.98)$$

where we have used the Δ function introduced by LC, defined in terms of Kronecker deltas as

$$\Delta_{jkl;m}^{(1)} = \delta_{-j+k+l,m} - \delta_{-j+k+l,-m} - \delta_{-j+k+l,2(N+1)-m}$$
$$+ \delta_{j-k+l,m} - \delta_{j-k+l,-m} - \delta_{j-k+l,2(N+1)-m}$$
$$+ \delta_{j+k-l,m} - \delta_{j+k-l,-m} - \delta_{j+k-l,2(N+1)-m} \qquad (1.99)$$
$$- \delta_{j+k+l,m} + \delta_{j+k+l,2(N+1)-m} - \delta_{j+k+l,2(N+1)+m},$$

and have exploited the fact that it is invariant under any permutation of the indices j, k, and l. The function $\Delta_{jkl;m}^{(2)}$, also defined by LC, is not needed for our simplified model. The Δ function ensures the conservation of lattice momentum—the conservation of momentum to within the non-uniqueness of the specification of the normal modes due to the fact that $\sin(nq_m) = \sin(nq_{2k(N+1)\pm m})$ for any integer k. The first Kronecker delta in each line is a condition of direct momentum conservation, and the other two are the so-called umklapp conditions where only lattice momentum is conserved.

As for the single resonator, we again try a steady-state solution, this time of the form

$$A_m(T) = a_m e^{i\left(\frac{\Omega_P}{2}\right)T}, \qquad (1.100)$$

so that the solutions to the EOM, after substitution of (1.100) into (1.95), become

$$u_n(t) = \epsilon^{1/2} \frac{1}{2} \sum_m \left(a_m \sin(nq_m) e^{i\left(1 + \frac{\epsilon\Omega_P}{2}\right)t} + c.c. \right) + O(\epsilon^{3/2}), \tag{1.101}$$

where all modes are oscillating at half the parametric excitation frequency.

Substituting the steady state solution (1.100) into the equations (1.98) for the time-varying amplitudes $A_m(T)$, we obtain the equations for the time-independent complex amplitudes a_m

$$\left[\Omega_P + 2d \sin^2 \left(\frac{q_m}{2} \right) - i \right] a_m - \frac{h}{2} a_m^* - \frac{3 + i\eta}{16} \sum_{j,k,l} a_j a_k a_l^* \Delta_{jkl;m}^{(1)} = 0. \tag{1.102}$$

Note that the first two terms on the left-hand side indicate that the linear resonance frequency is not obtained for $\Omega_P = 0$, but rather for $\Omega_P + 2d \sin^2 (q_m/2) = 0$. In terms of the unscaled parameters, this implies that the resonance frequency of the mth mode is $\omega_m = 1 - D \sin^2 (q_m/2)$, which to within a correction of $O(\epsilon^2)$ is the same as the expected dispersion relation

$$\omega_m^2 = 1 - 2D \sin^2 \left(\frac{q_m}{2} \right). \tag{1.103}$$

Equation (1.102) is the main result of the calculation. We have managed to replace N coupled differential equations (1.89) for the resonator coordinates $u_n(t)$ by N coupled algebraic equations (1.102) for the time-independent mode amplitudes a_m. All that remains, in order to obtain the overall collective response of the array as a function of the parameters of the original EOM, is to solve these coupled algebraic equations.

First, one can easily verify that for a single resonator ($N = j = k = l = m = 1$), the general equation (1.102) reduces to the single-resonator equation (1.73), we derived in § 1.3.4, as $\Delta_{111;1} = 4$. Next, one can also see that the trivial solution, $a_m = 0$ for all m, always satisfies the equations, though, as we have seen in the case of a single resonator, it is not always a stable solution. Finally, one can also verify that whenever for a given m, $\Delta_{mmm;j}^{(1)} = 0$ for all $j \neq m$, then a single-mode solution exists with $a_m \neq 0$ and $a_j = 0$ for all $j \neq m$. These single-mode solutions have the same type of elliptical shape of the single-resonator solution given in Eq. (1.74). Note that generically $\Delta_{mmm;m}^{(1)} = 3$, except when umklapp conditions are satisfied.

Additional solutions, involving more than a single mode, exist in general but are hard to obtain analytically. LC calculated these multi-mode solutions for the case of two and three resonators for the model they considered by finding the roots of the coupled algebraic equations numerically. We show some of their results to illustrate the type of behavior that occurs, although the precise details will be slightly different.

1.4.3
The response of very small arrays – Comparison of analytics and numerics

In Fig. 1.13 we show the solutions for the response intensity of two resonators as a function of frequency, for a particular choice of the equation parameters. The top graph
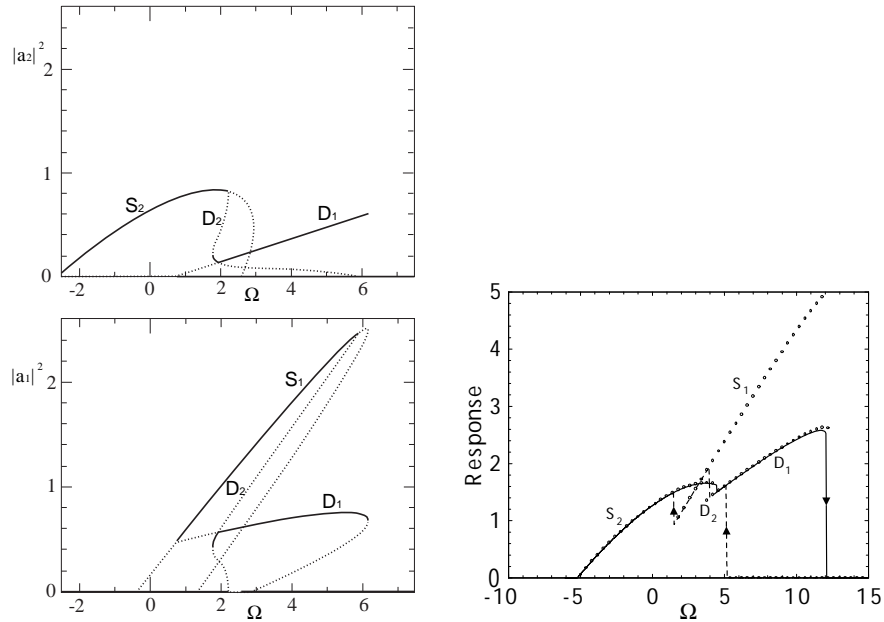
Fig. 1.13 Two resonators. Left: Response intensity as a function of frequency Ω_P, for a particular choice of the equation parameters. The top graph shows $|a_2|^2$, the bottom graph shows $|a_1|^2$. Solid curves indicate stable solutions and dashed curves indicate unstable solutions. The two elliptical single-mode solution branches are labeled S_1 and S_2. The two double-mode solution branches are labeled D_1 and D_2. Right: Comparison of stable solutions, obtained analytically (small circles), with a numerical integration of the equations of motion (solid curve - frequency swept up; dashed curve - frequency swept down) showing hysteresis in the response. Plotted is the averaged response intensity, defined in Eq. (1.104). Branch labels correspond to those on the left.

shows the square of the amplitude of the antisymmetric mode a_2, whereas the bottom graph shows the square of the amplitude of the symmetric mode a_1. Solid curves indicate stable solutions and dashed curves indicate unstable solutions. Two elliptical single-mode solution branches, similar to the response of a single resonator shown in Fig. 1.10 are easily spotted. These branches are labeled by S_1 and S_2. LC give the analytical expressions for these two solution branches. In addition, there are two double-mode solution branches, labeled D_1 and D_2, involving the excitation of both modes simultaneously. Note that the two branches of double-mode solutions intersect at a point where they switch their stability.

With two resonators there are regions in frequency where three stable solutions can exist. If all the stable solution branches are accessible experimentally then the observed effects of hysteresis might be more complex than in the simple case of a single resonator.

This is demonstrated on the right-hand side of Fig. 1.13 where the analytical solutions are compared with a numerical integration of the differential equations of motion (1.89) for two resonators. The response intensity, plotted here, is the time and space averages of the square of the resonator displacements

$$I = \frac{1}{N} \sum_{n=1}^{N} \left\langle u_n^2 \right\rangle, \tag{1.104}$$

where the angular brackets denote time average, and here $N = 2$. A solid curve shows the response intensity for frequency swept upwards, and a dashed curve shows the response intensity for frequency swept downwards. Small circles show the analytical response intensity, for the stable regions of the four solution branches shown in Fig. 1.13. With the analytical solution in the background, one can easily understand all the discontinuous jumps, as well as the hysteresis effects, that are obtained in the numerical solution of the equations of motion. Note that the S_1 branch is missed in the upwards frequency sweep and is only accessed by the system in the downwards frequency sweep. One could trace the whole stable region of the S_1 branch by changing the sweep direction after jumping onto the branch, thereby climbing all the way up to the end of the S_1 branch and then falling onto the tip of the D_1 branch or to zero. These kinds of changes in the direction of the sweep whenever one jumps onto a new branch are essential if one wants to trace out as much of the solution as possible—whether in real experiments or in numerical simulations.

1.4.4
Response of large arrays - Numerical simulation

LC integrated the equations of motion (1.88) numerically for an array of $N = 67$ resonators. The results for the response intensity (1.104) as a function of the unscaled parametric drive frequency ω_p are shown in Fig. 1.14. These results must be considered illustrative only, because the structure of the response branches will vary with changes to the model, and will also depend strongly on the chosen equation parameters. First of all, as in the case of a small number of beams, the overall height and width of individual response branches depend on the strength of the drive h, and on the nonlinear dissipation coefficient η. Furthermore, for example, if the coupling strength D is increased so that the width of the frequency response band become much larger than N times the width of a single-mode response, then very few multi-mode solutions exist, if any.

A number of the important features should be pointed out in the response. We concentrate on the solid curve in the figure, which is for frequency swept upwards. First, the response intensity shows features that span a range of frequencies that is large compared with the mode spacing (which is about 0.0006 for the parameters used). The reason for this is that as we follow a particular solution we skip over many others, as we saw for the S1 branch in the two-resonator case. Second, the variation of the response with frequency shows abrupt jumps, particularly on the high frequency
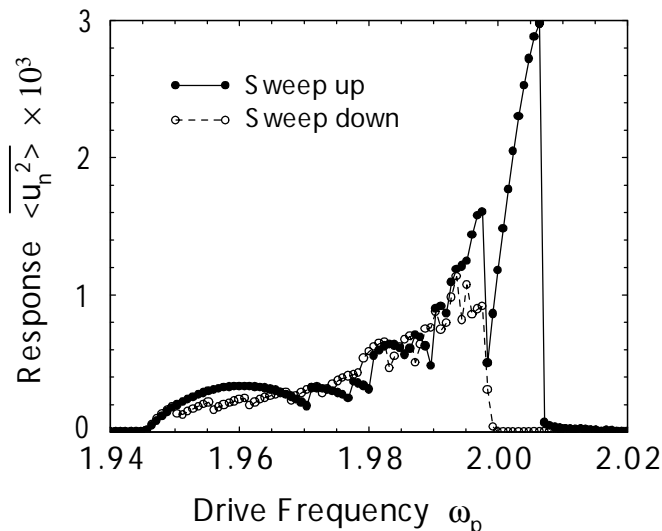
Fig. 1.14 Response intensity as a function of the driving frequency ω_p for $N = 67$ parametrically-driven resonators (solid curve - frequency swept up; dashed curve - frequency swept down). The response intensity is defined in Eq. (1.104). The response curve was obtained through numerical integration of the equations of motion (1.88).

side of the features as the frequency is raised. This happens as we reach saddle-node or other types of bifurcations where we lose the stability of the solution branch or the branch ends altogether. Third, the response extends to frequencies higher than the band edge for the linear modes, which would give a response only up to $\omega_p = 2.0$. This happens simply due to the positive Duffing parameter which causes frequency pulling to the right. Note that the downwards sweep is able to access additional stable solution branches that were missed in the upwards sweep. There is also no response above $\omega_p = 2.0$ in this case. This is because the zero displacement state is stable for $\omega_p > 2.0$, and the system will remain in this state as the frequency is lowered, unless a large enough disturbance kicks it onto another of the solution branches. The hysteresis on reversing the frequency sweep was not looked at in any experiment, and it would be interesting to test this prediction of LC in the future.

1.5
Amplitude equation description for large arrays

We finish this review by describing the approach used by BCL [61, 63] to obtain analytical results for large arrays by approaching them from the continuous limit of

infinitely-many degrees of freedom. We only summarize the main results of BCL and encourage the reader, who by now has all the required background, to refer to BCL [61] and to Kenig et al. [62] for details of the derivation and for thorough discussions of the results and their experimental consequences. We note that BCL studied the original system of equations (1.88), where both the parametric excitation and the damping are introduced in terms of the difference variables $u_{n+1} - u_n$. We stick to this model here, and leave it to the reader as an exercise to generalize the BCL derivation for the more general model equations (1.89) that we used in the previous section.

A novel feature of the parametrically-driven instability is that the bifurcation to standing waves switches from supercritical (continuous) to subcritical (discontinuous) at a wave number at or close to the critical one, for which the required parametric driving force is minimum. This changes the form of the amplitude equation that describes the onset of the parametrically-driven waves so that it no longer has the standard "Ginzburg-Landau" form [46]. The central result of BCL is this new scaled amplitude equation (1.112), governed by a single control parameter, that captures the slow dynamics of the coupled resonators just above the onset of parametric oscillations, including this unusual bifurcation behavior. BCL confirmed the behavior numerically and made suggestions for testing it experimentally. Kenig et al. [62] have extended the investigation of the amplitude equation to include such situations as time-dependent ramps of the drive amplitude, as opposed to the standard quasistatic sweeps of the control parameters. Although our focus here is on parametrically-driven NEMS & MEMS resonators, we should emphasize that the amplitude equation of BCL which we describe here should also apply to other parametrically-driven wave systems with weak nonlinear damping.

1.5.1
Amplitude equations for counter propagating waves

BCL scaled the equations of motion (1.88), as did Lifshitz and Cross [60], without assuming a priori that the coupling D is small, thus the scaled equations of motion that they solved were

$$
\ddot{u}_n + u_n + u_n^3 - \frac{1}{2}\epsilon(\dot{u}_{n+1} - 2\dot{u}_n + \dot{u}_{n-1})
$$
$$
+ \frac{1}{2}[D + \epsilon h \cos(2\omega_p t)](u_{n+1} - 2u_n + u_{n-1})
$$
$$
- \frac{1}{2}\eta[(u_{n+1} - u_n)^2(\dot{u}_{n+1} - \dot{u}_n) - (u_n - u_{n-1})^2(\dot{u}_n - \dot{u}_{n-1})] = 0, \qquad (1.105)
$$

Note also the way in which the pump frequency is specified as $2\omega_p$ in the argument of the cosine term, with an explicit factor of two (unlike what we did in section 1.4), and also without making any assumptions at this point regarding its deviation from twice the resonance. We also remind the reader that this, and all other frequencies, are measured in terms of the natural frequency of a single resonator which has been scaled to 1. The

first step in treating this system of equations analytically, is to introduce a continuous displacement field $u(x, t)$, and slow spatial and temporal scales, $X = \epsilon x$ and $T = \epsilon t$. One then tries a solution in terms of a pair of counter-propagating plane waves, at half the pump frequency, which is a natural first guess in continuous parametrically-driven systems, such as Faraday waves [46],

$$
\begin{aligned}
u(x, t) &= \epsilon^{1/2}[\left(A_+(X, T)e^{-iq_p x} + A_-^*(X, T)e^{iq_p x}\right)e^{i\omega_p t} + c.c.] \\
&+ \epsilon^{3/2}u^{(1)}(x, t, X, T) + \dots,
\end{aligned} \tag{1.106}
$$

where q_p and ω_p are related through the dispersion relation (1.103)

$$
\omega_p^2 = 1 - 2D \sin^2\left(\frac{q_p}{2}\right). \tag{1.107}
$$

By substituting this ansatz (1.106) into the equations of motion (1.105) and applying a solvability condition on the terms of order $\epsilon^{3/2}$, BCL obtained a pair of coupled amplitude equations for the counter-propagating wave amplitudes $A_\pm$

$$
\begin{aligned}
\frac{\partial A_\pm}{\partial T} &\pm v_g \frac{\partial A_\pm}{\partial X} = -\sin^2\left(\frac{q_p}{2}\right)A_\pm \mp i\frac{h}{2\omega_p}\sin^2\left(\frac{q_p}{2}\right)A_\mp \\
&- \left(4\eta\sin^4\left(\frac{q_p}{2}\right) \mp i\frac{3}{2\omega_p}\right)\left(|A_\pm|^2 + 2|A_\mp|^2\right)A_\pm,
\end{aligned} \tag{1.108}
$$

where the upper signs (lower signs) give the equation for A_+ (A_-) and

$$
v_g = \frac{\partial \omega_p}{\partial q_p} = -\frac{D\sin(q_p)}{2\omega_p} \tag{1.109}
$$

is the group velocity. This equation is the extension of Eq. (1.47) to many coupled resonators, only that now the parametric drive couples amplitudes of the two counter propagating waves A_+ and A_- instead of coupling A and A^*. A detailed derivation of the amplitude equations (1.108) can be found in Refs. [61, 63]. We should note that similar equations were previously derived for describing Faraday waves [64, 65].

By linearizing the amplitude equations (1.108) about the zero solution ($A_+ = A_- = 0$) we find that the linear combination of the two amplitudes that first becomes unstable at $h = h_c \equiv 2\omega_p$ is $B \propto (A_+ - iA_-)$—representing the emergence of a standing wave with a temporal phase of $\pi/4$ relative to the drive—while the orthogonal linear combination of the amplitudes decays exponentially and does not participate in the dynamics at onset. Thus, just above threshold a single amplitude equation should suffice, describing this standing wave pattern. We describe the derivation of this equation in the next section.

1.5.2
Reduction to a Single Amplitude Equation

Because, as we saw in § 1.3.4, nonlinear dissipation plays an important role in the saturation of the response to parametric excitation, it is natural to try to keep a balance

between the strength of this nonlinearity and the amount by which we drive the system above threshold. Assuming that the nonlinear damping is weak, we use it to define a second small parameter $\delta = \sqrt{\eta}$. This particular definition turns out to be useful if we then scale the reduced driving amplitude $(h - h_c)/h_c$ linearly with δ, defining a scaled reduced driving amplitude r by letting $(h - h_c)/h_c \equiv r\delta$. We can then treat the initial linear combination of the two amplitudes in (1.108) that becomes unstable by introducing a second ansatz,

$$
\begin{pmatrix} A_+ \\ A_- \end{pmatrix} = \delta^{1/4} \begin{pmatrix} 1 \\ i \end{pmatrix} B(\xi, \tau) + \delta^{3/4} \begin{pmatrix} w^{(1)}(X, T, \xi, \tau) \\ v^{(1)}(X, T, \xi, \tau) \end{pmatrix}
$$
$$
+ \delta^{5/4} \begin{pmatrix} w^{(2)}(X, T, \xi, \tau) \\ v^{(2)}(X, T, \xi, \tau) \end{pmatrix},
\tag{1.110}
$$

where $\xi = \delta^{1/2}X$ and $\tau = \delta T$. Substitution of this ansatz allows one to obtain the correction of the solution at order $\delta^{3/4}$

$$
\begin{pmatrix} w^{(1)} \\ v^{(1)} \end{pmatrix}
$$
$$
= \frac{1}{2\sin^2(q_p/2)} \left(-v_g \frac{\partial B}{\partial \xi} + i \frac{9}{2\omega_p} |B|^2 B \right) \begin{pmatrix} 1 \\ -i \end{pmatrix},
\tag{1.111}
$$

after which a solvability condition applied to the terms of order $\delta^{5/4}$ yields an equation for the field $B(\xi, \tau)$, which after scaling takes the form

$$
\frac{\partial B}{\partial \tau} = rB + \frac{\partial^2 B}{\partial \xi^2} + i\frac{2}{3}\left(4|B|^2 \frac{\partial B}{\partial \xi} + B^2 \frac{\partial B^*}{\partial \xi} \right) - 2|B|^2 B - |B|^4 B.
\tag{1.112}
$$

This is the BCL amplitude equation. It is governed by a single control parameter, the reduced drive amplitude r, and captures the slow dynamics of the coupled resonators just above the onset of parametric oscillations. The reader is encouraged to consult Ref. [61] for a more detailed account of the derivation of the BCL equation. The form of Eq. (1.112) is also applicable to the onset of parametrically driven standing waves in continuum systems with weak nonlinear damping, and combines in a single equation a number of effects studied previously [64–69].

1.5.3
Single Mode Oscillations

Now that this novel amplitude equation has been derived by BCL it can be used to study a variety of dynamical solutions, ranging from simple single-mode to more complicated nonlinear extended solutions, and after slight modifications also the dynamics of localized solutions. BCL used the amplitude equation to study the stability of single-mode steady-state solutions,

$$
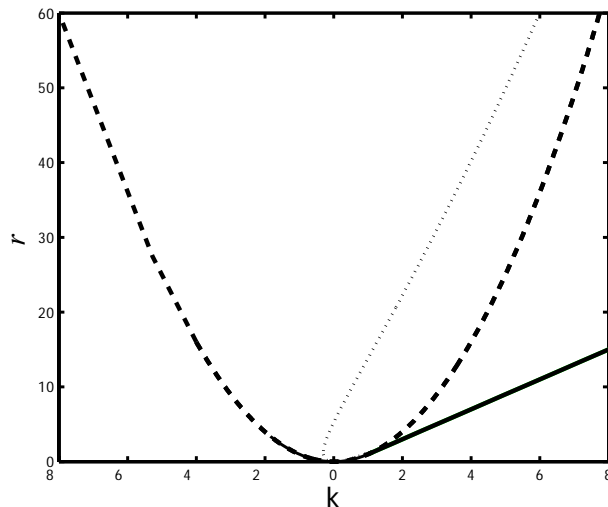B = b_k e^{-ik\xi},
\tag{1.113}
$$

Fig. 1.15 Stability boundaries of the single-mode solution of
Eq. (1.112) in the r vs. k plane. Dashed line: neutral stability bound-
ary below which the zero-state is stable. Dotted line: stability
boundary of the single-mode solution (1.113) above which the ar-
ray experiences an Eckhaus instability and switches to one of the
other single mode solutions. For $k > 1$ the bifurcation from zero
displacement becomes subcritical and the lower stability boundary
is the locus of saddle-node bifurcations (solid line).

i.e. standing-wave solutions that consist of a single sine-wave pattern with one of the
allowed wave vectors q_m. The wave vector k gives, in some scaled units, the difference
between the wave vector q_p, determined by the pump frequency through the dispersion
relation, and the wave vector $q_m = m\pi/(N+1)$, $m = 1 \ldots N$, of the actual mode
that is selected by the system.

A number of interesting results easily pop out if we simply substitute the single-
mode solution (1.113) into the BCL amplitude equation (1.112). From the linear terms
in the amplitude equation we find, as expected, that for $r > k^2$ the zero-displacement
solution is unstable to small perturbations of the form of (1.113), defining the parabolic
neutral stability curve, shown as a dashed line in Fig. 1.15. The nonlinear gradients
and the cubic term take the simple form $2(k-1)|b_k|^2 b_k$. For $k < 1$ these terms
immediately act to saturate the growth of the amplitude assisted by the quintic term.
Standing waves therefore bifurcate supercritically from the zero-displacement state.
For $k > 1$ the cubic terms act to increase the growth of the amplitude, and saturation
is achieved only by the quintic term. Standing waves therefore bifurcate subcritically
from the zero-displacement state. The saturated amplitude $|b_k|$, obtained by setting
Eq. (1.112) to zero, is given by

$$|b_k|^2 = (k-1) \pm \sqrt{(k-1)^2 + (r-k^2)} \geq 0. \tag{1.114}$$
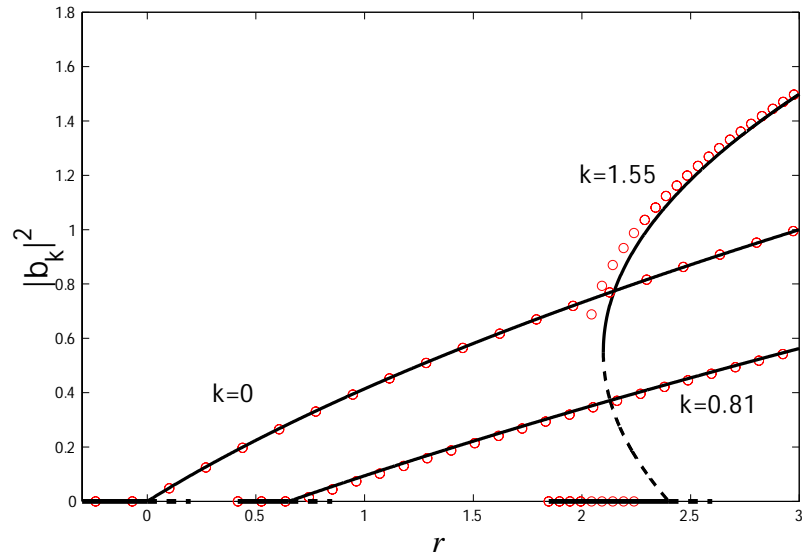
Fig. 1.16 Response of the resonator array plotted as a function of reduced amplitude r for three different scaled wave number shifts: $k = 0$ and $k = -0.81$, which bifurcate supercritically, and $k = 1.55$ which bifurcates subcritically showing clear hysteresis. Solid and dashed lines are the positive and negative square root branches of the calculated response in (1.114), the latter clearly unstable. Open circles are numerical values obtained by integration of the equations of motion (1.105), with $D = 0.25$, $\omega_p = 0.767445$, $\epsilon = 0.01$, and $\eta = 0.1$.

In Fig. (1.16) we plot $|b_k|^2$ as a function of the reduced driving amplitude r for three different wave number shifts k. The solid (dashed) lines are the stable (unstable) solutions of Eq. (1.114). The circles were obtained by numerical integration of the equations of motion (1.105). For each driving amplitude, the Fourier components of the steady state solution were computed to verify that only single modes are found, suggesting that in this regime of parameters only these states are stable.

BCL showed the power of the amplitude equation in predicting the first single-mode solution that should appear at onset as well as the sequence of Eckhaus instabilities that switch to other single-mode solutions as the reduced drive amplitude r is quasistatically increased. Kenig et al. used the amplitude equation to analyze more generally the question of pattern selection—predicting which oscillating pattern will be observed under particular experimental conditions from among all the stable steady-state solutions that the array of resonators can choose from. In particular they have considered experimental situations in which the drive amplitude r is changed abruptly or swept at rates that are faster than typical transient times. In all cases the predictions of the

amplitude equation are confirmed with numerical simulations of the original equations of motion (1.105). Experimental confirmation of these predictions is still not available.

Acknowledgments

Bibliography

1 M. L. Roukes. Plenty of room indeed. Scientific American, 285:42–49, 2001.

2 M. L. Roukes. Nanoelectromechanical systems face the future. Physics World, 14:25–31, 2001.

3 H. G. Craighead. Nanoelectromechanical systems. Science, 290:1532–1535, 2000.

4 Andrew N. Cleland. Foundations of Nanomechanics. Springer, Berlin, 2003.

5 K. L. Ekinci and M. L. Roukes. Nanoelectromechanical systems. Review of Scientific Instruments, 76:061101, 2005.

6 K. L. Ekinci, X. M. H. Huang, and M. L. Roukes. Ultrasensitive nanoelectromechanical mass detection. Appl. Phys. Lett., 84:4469–4471, 2004.

7 B. Ilic, H. G. Craighead, S. Krylov, W. Senaratne, C. Ober, and P. Neuzil. Attogram detection using nanoelectromechanical oscillators. Journal of Applied Physics, 95:3694–3703, 2004.

8 Y.T. Yang, C. Callegari, X.L. Feng, K.L. Ekinci, and M.L. Roukes. Zeptogram-scale nanomechanical mass sensing. Nano Letters, 6:583–586, 2006.

9 D Rugar, R Budakian, H J Mamin, Chui, and B W. Single spin detection by magnetic resonance force microscopy. Nature, 430:329–332, 2004.

10 Andrew N. Cleland and Michael L. Roukes. A nanometer-scale mechanical electrometer. Nature, 392:160, 1998.

11 Andrew N. Cleland and Michael L. Roukes. Nanoscale mechanics. In Proceedings of the 24th International Conference on the Physics of Semiconductors. World Scientific, 1999.

12 Keith C. Schwab, E. A. Henriksen, J. M. Worlock, and Michael L. Roukes. Measurement of the quantum of thermal conductance. Nature, 404:974–977, 2000.

13 Miles P. Blencowe. Quantum electromechanical systems. Physics Reports, 395:159–222, 2004.

14 Keith C. Schwab and Michael L. Roukes. Putting mechanics into quantum mechanics. Physics Today, 58(7):36–42, 2005.

15 Kimberly L. Turner, Scott A. Miller, Peter G. Hartwell, Noel C. MacDonald, Steven H. Strogatz, and Scott G. Adams. Five parametric resonances in a microelectromechanical system. Nature, 396:149–152, 1998.

16 Eyal Buks and Michael L. Roukes. Metastability and the casimir effect in micromechanical systems. Europhys. Lett., 54:220, 2001.

17 Dominik V. Scheible, Artur Erbe, Robert H. Blick, and Gilberto Corso. Evidence of a

nanomechanical resonator being driven into chaotic response via the ruelle–takens route. Applied Physics Letters, 81:1884–1886, 2002.

18 Wenhua Zhang, Rajashree Baskaran, and Kimberly L. Turner. Effect of cubic nonlinearity on auto-parametrically amplified resonant mems mass sensor. Sensors and Actuators A, 102:139–150, 2002.

19 Wenhua Zhang, Rajashree Baskaran, and Kimberly Turner. Tuning the dynamic behavior of parametric resonance in a micromechanical oscillator. Applied Physics Letters, 82:130–132, 2003.

20 Min-Feng Yu, Gregory J. Wagner, Rodney S. Ruoff, and Mark J. Dyer. Realization of parametric resonances in a nanowire mechanical system with nanomanipulation inside a scanning electron microscope. Physical Review B, 66:073406, 2002.

21 J. S. Aldridge and A. N. Cleland. Noise-enabled precision measurements of a duffing nanomechanical resonator. Physical Review Letters, 94:156403, 2005.

22 A. Erbe, H. Krommer, A. Kraus, R. H. Blick, G. Corso, and K. Richter. Mechanical mixing in nonlinear nanomechanical resonators. Applied Physics Letters, 77:3102–3104, 2000.

23 D. Rugar and P. Grütter. Mechanical parametric amplification and thermomechanical noise squeezing. Phys. Rev. Lett., 67:699, 1991.

24 Dustin W. Carr, Stephane Evoy, Lidija Sekaric, H. G. Craighead, and J. M. Parpia. Parametric amplification in a torsional microresonator. Applied Physics Letters, 77:1545–1547, 2000.

25 Dustin W. Carr, S. Evoy, L. Sekaric, H. G. Craighead, and J. M. Parpia. Measurement of mechanical resonance and losses in nanometer scale silicon wires. Applied Physics Letters, 75:920–922, 1999.

26 Eyal Buks and Bernard Yurke. Mass detection with a nonlinear nanomechanical resonator. Physical Review E, 74:046619, 2006.

27 R. Almog, S. Zaitsev, O. Shtempluck, and E. Buks. High intermodulation gain in a micromechanical duffing resonator. Appl. Phys. Lett., 88:213509, 2006.

28 X. L. Feng, Rongrui He, Peidong Yang, , and M. L. Roukes. Very high frequency silicon nanowire electromechanical resonators. Nano Letters, 7:1953–1959, 2007.

29 Robert B. Reichenbach, Maxim Zalalutdinov, Keith L. Aubin, Richard Rand, Brian H. Houston, Jeevak M. Parpia, and Harold G. Craighead. Third-order intermodulation in a micromechanical thermal mixer. J. MEMS, 14:1244–1252, 2005.

30 A. Husain, J. Hone, Henk W. Ch. Postma, X. M. H. Huang, T. Drake, M. Barbic, A. Scherer, , and M. L. Roukes. Nanowire-based very-high-frequency electromechanical resonator. Appl. Phys. Lett., 83:1240–1242, 2003.

31 Barry E. DeMartini, Jeffrey F. Rhoads, Kimberly L. Turner, Steven W. Shaw, and Jeff Moehlis. Linear and nonlinear tuning of parametrically excited mems oscillators. J. MEMS, 16:310–318, 2007.

32 Vera Sazonova, Yuval Yaish, Hande Üstünel, David Roundy, Tomás A. Arias, and Paul L. McEuen. A tunable carbon nanotube electromechanical oscillator. Nature, 431:284–287, 2004.

33 X. M. H. Huang, C. A. Zorman, M. Mehregany, and Michael L. Roukes. Nature, 421:496, 2003.

34 A. N. Cleland and M. R. Geller. Superconducting qubit storage and entanglement with nanomechanical resonators. Physical Review Letters, 93:070501, 2004.

35 H. B. Peng, C. W. Chang, S. Aloni, T. D. Yuzvinsky, and A. Zettl. Ultrahigh frequency nanotube resonators. Physical Review Letters, 97:087203, 2006.

36 M. C. Cross, A. Zumdieck, Ron Lifshitz, and J. L. Rogers. Synchronization by nonlinear frequency pulling. Physical Review Letters, 93:224101, 2004.

37 E. Buks and M. L. Roukes. Electrically tunable collective response in a coupled micromechanical array. J. MEMS, 11:802–807, 2002.

38 M. Sato, B. E. Hubbard, A. J. Sievers, B. Ilic, D. A. Czaplewski, and H. G. Craighead. Observation of locked intrinsic localized vibrational modes in a micromechanical oscillator array. Physical Review Letters, 90:044102, 2003.

39 M. Sato, B. E. Hubbard, A. J. Sievers, B. Ilic, D. A. Czaplewski, and Harold G. Craighead. Studies of intrinsic localized vibrational modes in micromechanical oscillator arrays. Chaos, 13:702–715, 2003.

40 M. Sato, B. E. Hubbard, A. J. Sievers, B. Ilic, and Harold G. Craighead. Optical manipulation of intrinsic localized vibrational energy in

cantilever arrays. Europhys. Lett., 66:318–323, 2004.

41 L. D. Landau and E. M. Lifshitz. Theory of Elasticity. Butterworth-Heinemann, Oxford, 3rd edition, 1986. §20 & 25.

42 B. Yurke, D. S. Greywall, A. N. Pargellis, and P. A. Busch. Theory of amplifier-noise evasion in an oscillator employing a nonlinear resonator. Phys. Rev. A, 51:4211–4229, 1995.

43 H. W. Ch. Postma, I. Kozinsky, A. Husain, and M. L. Roukes. Dynamic range of nanotube- and nanowire-based electromechanical systems. Appl. Phys. Lett., 86:223105, 2005.

44 L. N. Hand and J. D. Finch. Analytical Mechanics, chapter 10. Cambridge Univ. Press, Cambridge, 1998.

45 Steven H. Strogatz. Nonlinear dynamics and chaos, chapter 7. Addison-Wesley, Reading MA, 1994.

46 M. C. Cross and P. C. Hohenberg. Pattern formation outside of equillibrium. Rev. Mod. Phys., 65:851–1112, 1993.

47 Evoy, Carr, Sekaric, Olkhovets, Parpia, and Craighead. J. Appl. Phys., 86:6072, 1999.

48 Stav Zaitsev, Ronen Almog, Oleg Shtempluck, and Eyal Buks. Nonlinear dynamics in nanomechanical oscillators. Proceedings of the 2005 International Conference on MEMS,NANO and Smart Systems, pages 387–391, 2005.

49 R. Almog, S. Zaitsev, O. Shtempluck, and E. Buks. Noise squeezing in a nanomechanical duffing resonator. Physical Review Letters, 98:078103, 2007.

50 Inna Kozinsky, Henk W. Ch. Postma, Oleg Kogan, A. Husain, and Michael L. Roukes. Basins of attraction of a nonlinear nanomechanical resonator. Phys. Rev. Lett., 99:207201, 2007.

51 Itamar Katz, Alex Retzker, Raphael Straub, and Ron Lifshitz. Signatures for a classical to quantum transition of a driven nonlinear nanomechanical resonator. Phys. Rev. Lett., 99:040404, 2007.

52 I. Kozinsky, H. W. Ch. Postma, I. Bargatin, and M. L. Roukes. Tuning nonlinearity, dynamic range, and frequency of nanomechanical resonators. Appl. Phys. Lett., 88:253101, 2006.

53 L. D. Landau and E. M. Lifshitz. Mechanics. Butterworth-Heinemann, Oxford, 3rd edition, 1976. §27.

54 Rajashree Baskaran and Kimberly L Turner. Mechanical domain coupled mode parametric resonance and amplification in a torsional mode micro electro mechanical oscillator. J. Micromech. Microeng., 13:701–707, 2003.

55 Jeffrey F. Rhoads, Steven W. Shaw, Kimberly L. Turner, Jeff Moehlis Barry E. De-Martini, and Wenhua Zhang. Generalized parametric resonance in electrostatically actuated microelectromechanical oscillators. J. Sound Vib., 296:797–829, 2006.

56 Jeffrey F Rhoads, Steven W Shaw, and Kimberly L Turner. The nonlinear response of resonant microbeam systems with purely-parametric electrostatic actuation. J. Micromech. Microeng., 16:890–899, 2006.

57 S. C. Masmanidis, R. B. Karabalin, I. De Vlaminck, G. Borghs, M. R. Freeman, and M. L. Roukes. Multifunctional nanomechanical systems via tunably-coupled piezoelectric actuation. Science, 317:317–780, 2007.

58 E. Buks and M. L. Roukes. Electrically tunable collective response in a coupled micromechanical array. J. MEMS, 11:802–807, 2002.

59 Jeff Moehlis. Private communication.

60 Ron Lifshitz and M. C. Cross. Response of parametrically driven nonlinear coupled oscillators with application to micromechanical and nanomechanical resonator arrays. Physical Review B, 67:134302, 2003.

61 Yaron Bromberg, M. C. Cross, and Ron Lifshitz. Response of discrete nonlinear systems with many degreesof freedom. Physical Review E, 73:016214, 2006.

62 Eyal Kenig, Ron Lifshitz, and Michael C. Cross. Pattern selection in parametrically-driven arrays of nonlinear micromechanical or nanomechanical resonators. Preprint, 2008.

63 Yaron Bromberg. Response of nonlinear systems with many degrees of freedom. Master's thesis, Tel Aviv University, 2004.

64 A. B. Ezerskiĭ, M. I. Rabinovich, V. P. Reutov, and I. M. Starobinets. Spatiotemporal chaos in the parametric excitation of capillary ripple. Zh. Eksp. Teor. Fiz., 91:2070–2083, 1986. [Sov. Phys. JETP 64, 1228 (1986)].

65 S. T. Milner. Square patterns and secondary instabilities in driven capillary waves. J. Fluid Mech., 225:81–100, 1991.

66 H. Riecke. Stable wave-number kinks in parametrically excited standing waves. Europhys. Lett., 11:213–218, 1990.

67 Robert J. Deissler and Helmut R. Brand. Effect of nonlinear gradient terms on breathing localized solutions in the quintic complex ginzburg-landau equation. Phys. Rev. Lett., 81:3856–3859, 1998.

68 Peilong Chen and Kuo-An Wu. Subcritical bifurcations and nonlinear ballons in faraday waves. Phys. Rev. Lett., 85:3813–3816, 2000.

69 Peilong Chen. Nonlinear wave dynamics in faraday instabilities. Physical Review E, 65:036308, 2002.